A ZTF Search for Circumstellar Debris Transits in White Dwarfs: Six New Candidates, One with Gas Disk Emission, Identified in a Novel Metric Space

Soumyadeep Bhattacharjee[1,2] , Zachary P. Vanderbosch[1] , Mark A. Hollands[3] , Pier-Emmanuel Tremblay[3] , Siyi Xu (许偲艺)[4] , Joseph A. Guidry[5,13] , J. J. Hermes[5] , Ilaria Caiazzo[6] , Antonio C. Rodriguez[1] , Jan van Roestel[7] , Kareem El-Badry[8] , Andrew J. Drake[8], Benjamin R. Roulston[9] , Reed Riddle[8] , Ben Rusholme[10] , Steven L. Groom[10] , Roger Smith[11] , and Odette Toloza[12]

[1] Department of Astronomy, California Institute of Technology, 1200 East California Blvd, Pasadena, CA 91125, USA; sbhatta2@caltech.edu
[2] Department of Physics, Indian Institute of Science, Bengaluru, Karnataka 560012, India
[3] Department of Physics, University of Warwick, Coventry CV4 7AL, UK
[4] Gemini Observatory/NSF's NOIRLab, 950 N. Cherry Ave, Tucson, AZ 85719, USA
[5] Department of Astronomy & Institute for Astrophysical Research, Boston University, Boston, MA 02215, USA
[6] Institute of Science and Technology Austria, Am Campus 1, 3400 Klosterneuburg, Austria
[7] Anton Pannekoek Institute for Astronomy, University of Amsterdam, 1090 GE Amsterdam, The Netherlands
[8] Department of Astronomy, California Institute of Technology, 1216 E. California Blvd, Pasadena, CA 91125, USA
[9] Department of Physics, 8 Clarkson Ave, Potsdam, NY 13699, USA
[10] IPAC, California Institute of Technology, 1200 E. California Blvd, Pasadena, CA 91125, USA
[11] Caltech Optical Observatories, California Institute of Technology, Pasadena, CA 91125, USA
[12] Departamento de Física, Universidad Técnica Federico Santa María, Avenida España 1680, Valparaśo, Chile

Abstract

White dwarfs (WDs) showing transits from orbiting planetary debris provide significant insights into the structure and dynamics of debris disks, which are eventually accreted to produce metal pollution. This is a rare class of objects with only eight published systems. In this work, we perform a systematic search for such systems within 500 pc in the Gaia-eDR3 catalog of WDs using the light curves from the Zwicky Transient Facility (ZTF) and present six new candidates. Our selection process targets the top 1% most photometrically variable sources identified using a combined variability metric from ZTF and Gaia eDR3 photometry, boosted by a metric space we define using von Neumann statistics and Pearson-Skew as a novel discovery tool to identify these systems. This is followed by optical spectroscopic observations of visually selected variables to confirm metal pollution. Four of the six systems show long-timescale photometric variability spanning several months to years, resulting either from long-term evolution of transit activity or dust and debris clouds at wide orbits. Among them, WD J1013−0427 shows an indication of reddening during the long-duration dip. Interpreting this as dust extinction makes it the first system to indicate an abundance of dust grains with radius $\lesssim 0.3\,\mu$m in the occulting material. The same object also shows metal emission lines that map an optically thick eccentric gas disk orbiting within the star's Roche limit. For each candidate, we infer the abundances of the photospheric metals and estimate accretion rates. We show that transiting debris systems tend to have higher inferred accretion rates compared to the general population of metal-polluted WDs. Growing the number of these systems will further illuminate such comparative properties in the near future. Separately, we also serendipitously discovered an AM Canis Venaticorum showing a very long-duration outburst—only the fourth such system to be known.

Unified Astronomy Thesaurus concepts: White dwarf stars (1799); Transits (1711); Debris disks (363); Circumstellar gas (238); Variable stars (1761)

1. Introduction

White dwarfs are the end states of all low to moderately massive stars in our Galaxy, including the Sun and essentially all currently known planet-hosting stars.[14] In recent years, many direct and indirect signatures of planetary systems orbiting white dwarfs have been observed, with over 40% of

---

[14] See NASA Exoplanet Archive: https://exoplanetarchive.ipac.caltech.edu/.

white dwarfs cooler than 20,000 K exhibiting atmospheric pollution by heavy elements (Zuckerman et al. 2003, 2010; Koester et al. 2014; Ould Rouis et al. 2024). This metal pollution is widely interpreted as resulting from the active accretion of planetary bodies that survived post-main sequence evolution but were then gravitationally perturbed by larger surviving planets onto highly eccentric orbits and tidally disrupted upon entering the Roche radius of the white dwarf (Debes & Sigurdsson 2002; Jura 2003). The metal pollution carries rich information about the bulk composition of the accreted planetary material (e.g., Zuckerman et al. 2007; Dufour et al. 2010; Melis et al. 2011; Farihi et al. 2013; Bauer & Bildsten 2019; Putirka & Xu 2021; Swan et al. 2023; Rogers et al. 2024). Subsets of metal-polluted white dwarfs also exhibit a detectable infrared excess emitted by a warm, dusty debris disk (Zuckerman & Becklin 1987; Jura et al. 2007; Mullally et al. 2007; Farihi et al. 2008; Wilson et al. 2019; Dennihy et al. 2020a; Xu et al. 2020; Lai et al. 2021; Wang et al. 2023), emission lines from a gaseous component of the debris disk (Gänsicke et al. 2006; Dennihy et al. 2020b; Manser et al. 2020; Gentile Fusillo et al. 2021a; Owens et al. 2023), or absorption lines from circumstellar gas (Debes et al. 2012; Xu et al. 2016; Steele et al. 2021; Vanderbosch et al. 2021).

Another signature of planetary debris around white dwarfs is the attenuation of white dwarf flux due to transiting planetary debris. Such observations are expected if the debris disk is viewed edge on. The first such system, WD 1145+017,[15] was reported by Vanderburg et al. (2015) with debris orbital periods ranging from 4.5 to 4.9 hr. Three additional white dwarfs are confirmed to exhibit periodically recurring planetary debris transits: WD J0139+5245, with a period around 100 days (Vanderbosch et al. 2020), WD J0328−1219, with two detected periods of 9.94 hr and 11.2 hr (Vanderbosch et al. 2021), and WD 1054−226, with a dominant period around 25 hr (Farihi et al. 2022). In addition, a study using variability metrics based on Gaia DR2 and public DR3 Zwicky Transient Facility (ZTF; Bellm et al. 2019; Masci et al. 2019) photometry identified four more white dwarfs whose photometric variability is likely the result of transiting planetary debris (Guidry et al. 2021), but debris orbital periods have yet to be determined for these objects. Detecting transits is expected to be difficult; only about 1% of bright, metal-polluted white dwarfs show periodic transits in Transiting Exoplanet Survey Satellite (TESS; Robert et al. 2024). Here we want to point out that, recently, similar quasi-periodic deep transits were discovered in a central stellar system of a planetary nebula, WeSb 1 (Bhattacharjee et al. 2025a; Budaj et al. 2025). This candidate wide binary system can potentially represent initial stages of debris disk formation around white dwarfs and their companions.

The methodology presented by Guidry et al. 2021 showed great promise for the detection of white dwarfs with transiting debris candidates in data sets that are sparsely sampled relative to other surveys that have detected such objects, namely Kepler/K2 with 1 and 30-minutes cadences (e.g., Vanderburg et al. 2015) and TESS with 20 s, 2 minutes, and 30 minutes cadences (e.g., Vanderbosch et al. 2021; Farihi et al. 2022). Despite only analyzing about 66,000 white dwarfs within 200 pc and with Gaia photometric effective temperatures between 7000 and 16,000 K, Guidry et al. (2021) identified seven transiting debris systems in their sample, five of which were previously unknown at the time.

In this work, we present a dedicated search for transiting planetary debris at white dwarfs using more recent Gaia (eDR3) and ZTF (DR10)[16] photometry, but this time exploring and identifying a wider variety of variability metrics that are better suited to distinguishing transiting debris from other types of photometrically variable white dwarfs. In Section 2 we present our sample selection procedures and the variability metrics we apply to identify transiting debris candidates. In Section 3 we describe the follow-up observations we acquired for six new transiting debris candidates. In Section 4 we present the results of our search and spotlight each individual new transiting debris candidate. In Section 5, we present further analyses on WD J1013−0427, the first white dwarf to show significantly color-dependent transits along with gaseous emission. In Section 6, we compare the accretion rates of the transiting debris objects (from this and previous works) with other metal polluted white dwarfs and discuss the implications. Finally, we present our conclusion with a brief discussion on future direction in Section 7.

2. Selection Methods for New Transiting Debris Candidates

To conduct our search for new transiting planetary debris candidates, we follow closely the methodology described in Guidry et al. (2021, hereafter G21). This involves defining a subset of the Gaia eDR3 white dwarf catalog (Gentile Fusillo et al. 2021b) using several quality cuts (Section 2.1), cross matching with the ZTF light curve database to obtain epochal photometry (Section 2.2), and then calculating several variability metrics based on Gaia and ZTF photometry to identify the most variable objects in our sample (Section 2.4), and those that may be candidates for transiting planetary

---

[15] Naming convention: We follow the B1950 convention for three objects: WD 1145+017, WD 1054-226, and WD 1232+563 as they are well known in the literature by these names. For the others, we follow the format of "WD JHHMM+DDMM" (with coordinates at J2000). Where an abbreviation is needed (for example inside figures for lack of space), we instead use "JHHMM."

[16] This was the latest data release during which most of the work and target identification was carried out. A newer search using ZTF DR23 or later would add at least 4 yr of new survey photometry and potentially lead to more detections of transiting debris candidates.

Table 1
Sample Size After Each Selection or Decontamination Process

Process	Number
Gaia EDR3 white dwarf catalog	1.28 million
White dwarf probability $P_{WD} > 0.75$	359,073
Gaia astrometric and photometric cuts (see Section 2.1)	116,796
ZTF cross match	79,268
Automated Gaia decontamination (see Section 2.3)	59,459
$\geqslant$20 good ZTF detections in g- or r-bands	56,065
Top 1% sample after manual decontamination (see Section 2.5)	560

debris. We have made a few modifications to the G21 methodology to make our search more efficient, and attempt to identify light curve metrics that can more easily pick out transiting debris systems from other types of photometrically variable white dwarfs. We describe the selection methodology in the subsequent subsections. A summary of the exercise has been provided in Table 1.

2.1. Gaia Subset Selection

Our starting point for candidate selection is the Gaia eDR3 white dwarf catalog with 1.28 million sources (Gentile Fusillo et al. 2021b), 359,073 of which have probabilities for being a white dwarf $P_{WD} > 0.75$. Gaia eDR3 contains data with observations from 2014 July 25 to 2017 May 28, spanning a period of 34 months. We employ several astrometric and photometric quality cuts on the catalog (see Appendix A for a complete list) to generate a clean subset containing high-likelihood white dwarfs.

Many of our quality cuts are similar to those employed by G21, but with some notable differences. We increased the distance limit to 500 pc (PARALLAX $>$ 2 mas) instead of 200 pc, and we did not impose any direct restriction on white dwarf temperature or color, whereas G21 only looked at white dwarfs with photometric temperatures from Gentile Fusillo et al. (2019) between 7000 and 16,000 K. Also, as recommended in Gentile Fusillo et al. (2021b), we required $P_{WD} > 0.75$ to exclude low-confidence white dwarfs, and we used the Gaia BP/RP excess factor corrected for color dependence (Riello et al. 2021) to require |PHOT_BP_RP_EXCESS_FACTOR_CORRECTED| $< 2.0 \times$ SIGMA_EXCESS_FACTOR (see Appendix A for a more detailed description of these parameters). These cuts result in a subset with 116,796 Gaia eDR3 sources, a factor of about 2.5 increase in the Gaia-only subset defined in G21.

2.2. ZTF Photometry

The ZTF is a 47 deg^2 field-of-view camera attached to the 48 in Samuel Oschin telescope at Palomar Observatory. In operation since 2018 March, ZTF Phase I (2018 March—2020 September) observed the entire northern sky in g- and r-bands at declinations $\delta > -30$ deg with a three night cadence, while ZTF Phase II (2020 October—2023 September) observed with a two-night cadence. For each source in the Gaia subset with $\delta > -30$ deg (about 84, 100), we performed a 3″-radius cone search centered on the Gaia eDR3 coordinates using the ztfquery Python package (Rigault 2018) to obtain public DR10 g- and r-band light curves from the the NASA/IPAC Infrared Science Archive (IRSA) database. ZTF DR10 covers the time period from 2018 March 17 to 2022 January 5, or about 3.8 yr, an increase of about 1.8 yr compared to the ZTF DR3 photometry used in G21. We retrieved ZTF light curves for 79,268 objects.

Following recommendations given in the ZTF online documentation[17] and the ZTF Data System Explanatory Supplement,[18] we filter out poor quality ZTF detections by requiring that any ZTF data point must meet the following criteria: CATFLAGS = 0, |SHARP| < 0.25, CHI < 2 and MAG<LIMITMAG−1.0. After these cuts are applied, we also require that the LIMITMAG for each data point is at least 1.0 mag fainter than the median magnitude of the light curve in a given passband for each object. The LIMITMAG constraints help to remove spuriously bright data points on nights with relatively poor detection thresholds due to poor weather or bright sky background.

2.3. Automated ZTF Decontamination

We then ran an automated decontamination routine for every source with ZTF data to flag objects likely to have spurious photometry due to nearby stars. We used the same criteria defined in Appendix B of G21 to determine whether any surrounding stars are near or bright enough to a source to cause significant contamination. The criteria are: (i) all stars between 0″–5″ and 5″–7″.5 from the target should be at least 2 and 1 mag fainter, respectively (ii) stars between 7″.5 and 12″ should not be more than 2 mag brighter, and (iii) there should be no stars of magnitude $\leqslant$13 and $\leqslant$10 within 30″ and 60″ from the target, respectively. We initially queried the Panoramic Survey Telescope and Rapid Response System (Pan-STARRS1 or PS1, Chambers et al. 2016; Magnier et al. 2020) DR2 mean object catalog to search for the nearby stars. We chose PS1 at first because the photometric depth and filter passbands of the survey closely match those of ZTF, allowing for a more accurate assessment of contamination in the ZTF g- and r-bands.

We noticed, however, that one of the known transiting debris systems, WD 1054–226 (Farihi et al. 2022), was being flagged as contaminated by our routines even though it lacked

---

[17] https://irsa.ipac.caltech.edu/data/ZTF/docs/releases/ztf_release_notes_latest
[18] https://irsa.ipac.caltech.edu/data/ZTF/docs/ztf_explanatory_supplement.pdf

any surrounding stars close or bright enough to cause a problem. Several other objects exhibited similar contamination anomalies, many of which had high proper motions (e.g., WD 1054–226 has a total proper motion of $\mu = 308$ mas yr^{-1}). PS1 only groups single-epoch detections within a 1″ radius to create entries in the mean object catalog (Chambers et al. 2016; Flewelling et al. 2020), so objects with high proper motions that can shift by more than 1″ throughout the PS1 observing baseline (2009–2014, thus $\mu \gtrsim 200$ mas yr^{-1}) can potentially have two or more entries in the PS1 mean object table. These extra entries are interpreted as nearby contaminants by our decontamination routine, leading to the anomalous flagging of these sources.

This prompted us to instead use Gaia eDR3 for the decontamination process, since it measures and accounts for proper motions when generating source catalogs. The same criteria as described previously were applied using the Gaia G-band magnitude (PHOT_G_MEAN_MAG) to compare each source with the surrounding objects. We successfully recovered WD 1054–226 as a clean source, as well as several other high proper motion sources. Out of the 79,268 Gaia+ZTF sources, we determined 59,459 to be low risk for contamination according to our criteria.

2.4. Variability Metrics

To assess photometric variability in our decontaminated Gaia+ZTF sample, we applied several variability metrics to both the Gaia and ZTF photometry. We began by using variability metrics similar to those defined in G21, namely the Gaia metric (V_G), and the combined ZTF metric (V_{ZTF}). The Gaia metric is defined as

$$V_G = \frac{\sigma_G}{\langle G \rangle} \sqrt{n_{obs}} \qquad (1)$$

where σ_G, $\langle G \rangle$ and n_{obs} correspond to PHOT_G_MEAN_FLUX_ERROR, PHOT_G_MEAN_FLUX and PHOT_G_N_OBS in the Gaia eDR3 catalog, respectively. The ZTF metric is defined as

$$V_{ZTF} = MAX(\overline{V}_\sigma, \overline{V}_\delta) \qquad (2)$$

where $\overline{V}_\sigma$ and $\overline{V}_\delta$ are the standard deviation (σ) and average point-to-point scatter (δ)[19] of the ZTF light curves, respectively. These metrics represent the weighted average of the σ and δ calculated in each ZTF filter g and r, where we use the number of observations acquired in each filter as the weighting factor. So for a given object:

$$\overline{V}_\sigma = \frac{n_g V_{\sigma,g} + n_r V_{\sigma,r}}{n_g + n_r}, \qquad (3)$$

$$\overline{V}_\delta = \frac{n_g V_{\delta,g} + n_r V_{\delta,r}}{n_g + n_r} \qquad (4)$$

We calculate the σ and δ metrics after converting the ZTF light curves from magnitudes to units of flux change relative to the median magnitude in each filter (normalized relative flux), and only for the 56,065 objects that have at least 20 good-quality points in one or both bands. We use two statistical measures of the light curve scatter to assess variability because, as shown in G21 (see their Figure 8), variability occurring on timescales that are slow relative to the ZTF sampling rate of 1–3 days will tend to produce larger σ than δ metrics, while variability occurring on timescales faster than the ZTF sampling rate will produce similar σ and δ metrics. Calculating both and taking the maximum value as V_{ZTF} ensures that the ZTF metric serves as a useful proxy for variability across a broad range of timescales, while giving us a simple method to distinguish fast and slow variables.

As shown in Figure 1 (and also Figure 1 of G21), the raw V_G, V_σ, and V_δ metrics for the objects show increasing trends as a function of their magnitudes in the respective bands. This is expected since fainter sources will have more photometric noise. Our goal is to find sources with an excess of photometric scatter relative to non-variable sources of similar magnitude, so we remove these trends by fitting the metrics with an degree-eight polynomial as a function of the median magnitudes in the respective bands. Before fitting with the polynomial function, we perform 10 iterative 3σ clippings of the data to prevent photometrically variable or contaminated sources from affecting the fit. In spite of our automated decontamination routine, we expect some contaminated sources to remain. We then subtract the polynomial fits from the metric values. This detrending step is done independently for each metric and ZTF filter.

After subtraction, we still find a residual trend in the scatter of each metric, showing increasing scatter with increasing magnitude. We remove this trend slightly differently from G21, where the standard deviation of the metrics within suitable magnitude bins was taken as a measure of the scatter. We instead take the median absolute deviation (MAD) as the measure of the scatter for each bin, which is less affected by outliers. We chose bins of width 0.2 mag, and only considered bins that had at least 20 data points. To further mitigate the impact of highly variable sources, we performed an upper 5σ clipping of the data in each bin before calculating the MAD. We fit the trend of MAD versus magnitude for each metric with an exponential function, again doing this independently for each ZTF filter, and then normalized each metric by the respective fit. This results in the metrics all being in a common, unitless system that quantifies how many median absolute deviations each object is above or below the average metric value at a given magnitude. In this system, larger metric values are a proxy for photometric variability.
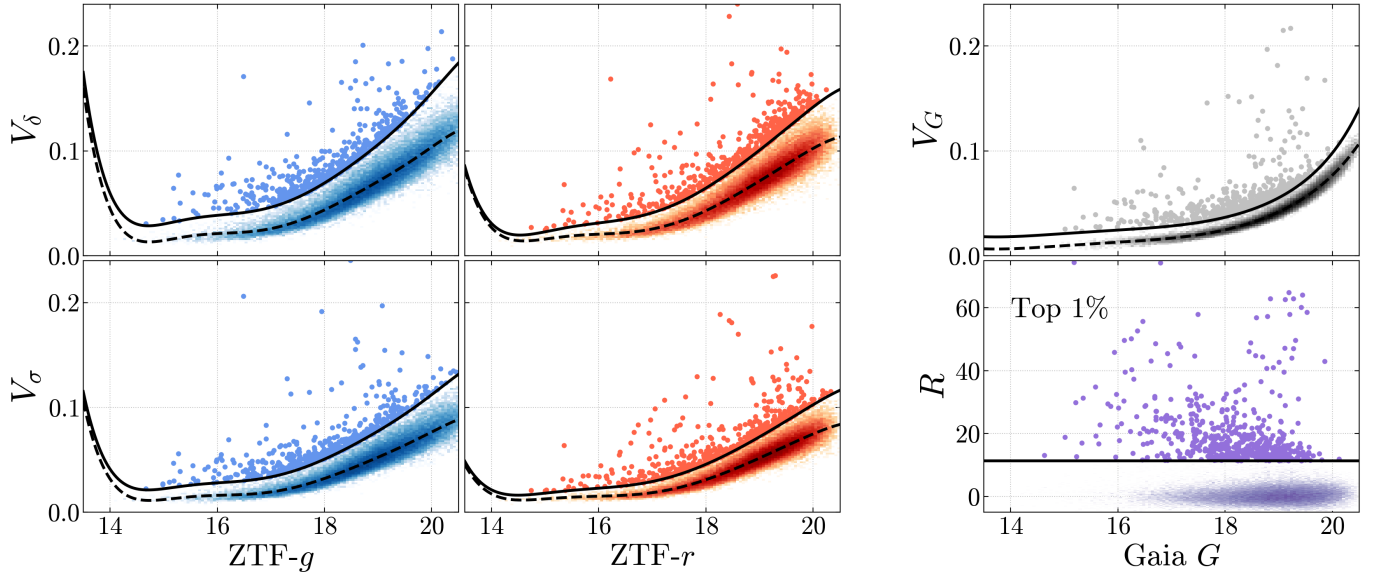
---

[19] $\delta = \sqrt{\frac{\sum_i (f_{i+1} - f_i)^2}{N-1}}$, where f_i are the relative flux values and N is the number of data points for a given object.

Figure 1. Summary of the metrics detrending and selection cut. Left and Middle panels: The V_δ and V_σ for the ZTF objects as a function of their respective magnitudes for g (left) and r (middle) bands. The dashed line shows the eight-degree polynomial fit to the overall trend with magnitude. The solid line shows the individual top 1% cuts with the exponential fit to the trend in the metric spread (with magnitude, after subtracting the polynomial fit) accounted for. Right Panel: The top figure shows the same for V_G. The bottom panel shows the final Rank metric and the 1% cut. The vertical axes have been truncated for better visualization. Only the objects passing all the decontamination tests are shown.

At this stage, we combine the detrended and normalized σ and δ metrics calculated in each ZTF filter as shown in Equations (3) and (4), and then calculate the combined ZTF metric as shown in Equation (2). Similar to G21, we then assign a final variability rank R to each object by combining the Gaia and ZTF metrics:

$$R = V_G + V_{ZTF} \qquad (5)$$

The bottom right panel in Figure 1 shows the distribution of R as a function of Gaia G. This final metric is mostly free of any systematic trends.

Unlike G21, we do not include ZTF alerts in the definition of R. We found the alerts to have a fairly strong magnitude bias, showing up more frequently in brighter objects. Among our Gaia+ZTF sample, just 417 objects have good-quality alerts and a median G-band magnitude of 17.5, whereas objects within the top 1% highest R values have a median G-band magnitude of 18.2 mag. Therefore, we primarily ignore the alerts to prevent skewing the variability rank towards brighter sources, though we have other concerns with using alerts as well. ZTF alerts are generated from difference images, the difference between a ZTF science and reference image. The reference images were built up from multiple science exposures acquired during the first year of ZTF operations. If for some reason an object was significantly brighter or fainter than average in the images used to generate the reference image, e.g., due to some transient or long-term variability, it may end up triggering a large number of alerts in

observations of subsequent years, even if the object is no longer variable at high-enough amplitudes to trigger alerts. Conversely, some objects might not have any alerts even if they are variable, simply because they may not be observed at the best time, e.g., during the peak of a pulsation or the bottom of an eclipse. Thus, we ignore the alerts when calculating the variability rank to help avoid such selection effects.

2.5. Final Decontamination and the Top 1% Sample

Assuming that we will be most likely to find new transiting debris candidates among sources that exhibit the most photometric variability, we now define our sample of interest as the sources with the top 1% highest variability rank, R. The initial list had around 680 sources. But, we noticed that for several objects among them, V_{ZTF} was significantly higher than V_G. We suspected that these might be objects with "bad" ZTF images, artificially inflating the ZTF metric. To weed most of them out, we visually checked the ZTF images of the objects that were within the top 1% only in terms of V_{ZTF} but not in terms of V_G. We indeed found several cases of contaminated ZTF images which include nearby bright stars that were missed by our automated routines, bad CCD pixel columns crossing the stellar point-spread function, and instrumental optical artifacts such as ghosts and internal reflections. We remove these objects from our list of highly variable sources. In total, we inspected the ZTF images of 171 objects and, among them, discarded 120 objects from the initial list due to bad ZTF images. This resulted in our final sample of top 1% objects in terms of R, consisting of

Table 2
Known Confirmed and Candidate Transiting Debris Systems Recovered

Name	Gaia eDR3 ID	References
WD 1145+017	3796414192429498880	Vanderburg et al. (2015)
WD J0139+5245	407197396840413696	Vanderbosch et al. (2020)
WD J0328−1219	5161807767825277184	Vanderbosch et al. (2021)
WD 1054−226	3549471753507182592	Farihi et al. (2022)
WD J0107+2107	2790417540424293120	Guidry et al. (2021)
WD J0347−1802	5107322396824711680	Guidry et al. (2021)
WD J0923+4236	817461778282929664	Guidry et al. (2021)
WD 1232+563	1571584539980588544	Guidry et al. (2021)
	...	Hermes et al. (2025)

560 sources. We consider only these objects in all subsequent analyses.

We cross-matched the sample with catalogs of known variable white dwarfs: ZZ Cetis (Córsico et al. 2019; Vincent et al. 2020; Guidry et al. 2021; Romero et al. 2022; Vanderbosch et al. 2022), Rotators (Kilic et al. 2021; Reindl et al. 2021, 2023, I. Caiazzo et al. 2025, in preparation), CVs (Ritter & Kolb 2003), and Binaries (van Roestel 2025, private communication). Additionally, we performed SIMBAD queries to infer the variability types of the objects not listed in the above-mentioned catalogs. All the previously identified transiting debris systems (summarized in Table 2) features in the top 1% list. We also recovered 77 previously known ZZ Cetis, 36 CVs, 4 Rotators, and 56 Binaries in our top 1% sample. We found more than 200 new likely pulsating white dwarfs lying in the ZZ Ceti instability strip, as well as several other new variables potentially belonging to each of the other variability types, though confirmatory follow-ups have not been performed. We are in the process of follow-up observations of several of these objects which are expected to be part of future papers.

2.6. A Unique Parameter Space for Identifying Candidate Transiting Debris Systems

In an attempt to increase the efficiency of identifying new transiting debris candidates, we also explore additional light curve variability metrics that quantify the timescales and flux asymmetry of an object's variability. Such metrics have already been used successfully to identify and characterize different populations of sources such as microlensing candidates (Rodriguez et al. 2022), young stellar objects (Cody et al. 2014; Hillenbrand et al. 2022), and variable planetary nebulae (Bhattacharjee et al. 2025a; Bhattacharjee et al. 2025b). In this work, we use the Von Neumann Metric (hereafter η) and the Pearson second coefficient of skew (hereafter S_P), defined as:

$$\eta = \left(\frac{\delta}{\sigma}\right)^2 \tag{6}$$

$$S_P = \frac{\widetilde{m} - \overline{m}}{\sigma}, \tag{7}$$
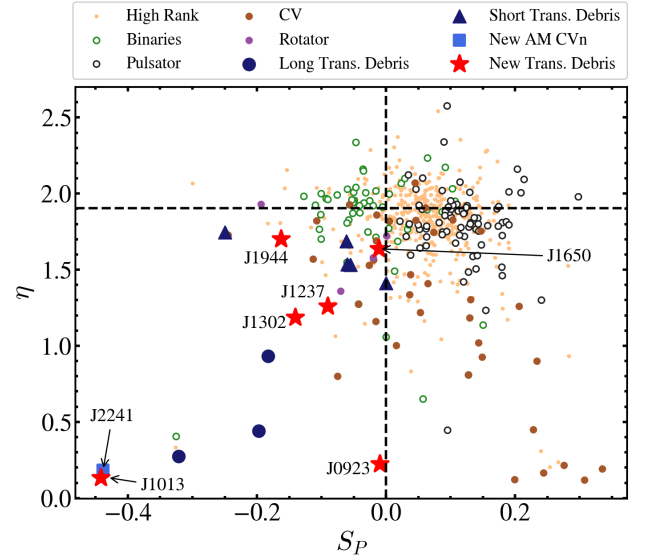
Figure 2. Position of the ZTF light curves in the η–S_P space for all the white dwarfs within top 1% R (orange points), and the known variable types within that list: Binaries (green circles), Pulsators (black circles), CVs (brown points), and the previously known (blue points and triangles) and new candidate (red stars) transiting debris systems. The transiting debris systems tend to lie in the third quadrant ($\eta < 1.9$ and $S_P < 0$), with the long and short-timescale systems having low and high η values, respectively. We mark the six new candidates being reported in this work by their names, and also the serendipitously discovered long-duration outbursting AM CVn (blue square). See Section 4 for the details about these objects.

where, $\widetilde{m}$ and $\overline{m}$ are the median and mean of the timeseries m, respectively. Unlike the previous excess-scatter metrics, we calculate these metrics using the light curve magnitude values instead of the relative flux values. This change resulted from experimentation with the metric values, which showed better performance with magnitudes owing to the logarithmic scale (thus more resistant to outliers). Objects with irregular variability resolved by ZTF are expected to have lower-than-average values of η. Objects undergoing dips (outbursts) are expected to have negative (positive) S_P values.

Figure 2 shows the position of all the white dwarfs featured in the top 1% in terms of the R metric (560 sources) in the η–S_P space. For convenience of presentation, we classify the variables into the following broad types: Binaries, Pulsating white dwarfs (ZZ Cetis and DBVs, Pulsator), Cataclysmic variable (CV), Rotational modulators (Rotator), and transiting debris. We further classified the transiting debris class into two observational classes: long and short timescale variables. These having timescale of variability greater than and less than approximately a few days to a week (i.e., the ZTF cadence), respectively (the definition of short and long timescale can be extended to other surveys with the respective survey cadence). We note here that the boundary between short and long-timescale transiting debris systems is shrinking as these objects

often tend to show variability on both timescales (Aungwerojwit et al. 2024 and also this work).

Broadly, different regions in the η–S_P parameter space are seen to be populated by different kinds of variable white dwarfs. For example, the light curves of CVs are often characterized by outbursts that push them toward positive S_P values. CV outbursts can last anywhere from days to years, (for examples, see Inight et al. 2023), which results in a broad range of η metrics. Meanwhile, pulsating white dwarfs (e.g., ZZ Cetis and DBVs) are all characterized by short timescale variability (2–20 minutes), mostly under-sampled by ZTF, that can range from sinusoidal to sharply peaked (e.g., see Guidry et al. 2021; Vanderbosch et al. 2022). This causes pulsating white dwarfs to cluster near the median η value of the sample, but with S_P shifted towards positive values. Binary systems are mostly clustered around the sample-median η value, but eclipsing systems can produce ZTF light curves with negative S_P values.

The transiting debris systems, with irregular dip-like variability, predominantly occupy the third quadrant (lower left) in this space. Figure 2 also includes the new candidates found in this work, details about which shall be discussed later in this paper (Section 4.1). We see that the quadrant containing the transiting debris candidates is less contaminated by other kinds of variables. This suggests that the η–S_P metric space can help with more efficient identification of white dwarfs with transiting debris-like light curves. The long-timescale transiting debris systems tend to have lower η values (primarily due to reduced δ metric value) than the short-timescale owing to better resolution of the variability with the ZTF sampling rate. This can be used to have a first guess about the variability timescale of the objects, which can in turn help in planning photometric follow-up observations.

3. Follow-up Observations

Using the metrics described above, we identified several objects within the third quadrant of the η–S_P space suitable for follow-up observations to determine whether they exhibit any characteristics in high-speed time series photometry or low-resolution spectroscopy that would indicate the presence of transiting planetary debris. We describe the time series photometry in Section 3.1 and the low-resolution spectroscopy in Section 3.2, and provide summaries of the observations in Tables 3 and 4.

3.1. Time Series Photometry

Palomar/CHIMERA. We carried out time series photometry at Palomar Observatory using the Caltech High Speed Multicolor Camera (CHIMERA; Harding et al. 2016) attached at prime focus of the 200-in Hale Telescope. We used the g- and r-band filters on the blue and red arms of the instrument, respectively, with exposures times of 5 or 10 s. We used

Table 3
Time Series Photometry Observations

Name WD	UT Date	Facility	Duration (hr)	t_{exp} (s)	Filters
J0923+7326	2021 Jun 8	McD	2.00	10	BG40
	2021 Jun 9	McD	1.51	20	BG40
J1013−0427	2022 Dec 25	PTO	3.99	40	BG40
	2023 Jan 25	P200	1.95	10	g
	⋯	P200	1.81	10	r
	2023 Jan 26	P200	2.01	10	$g + r$
J1237+5937	2023 Jan 27	P200	1.67	20	g
	⋯	P200	1.51	20	r
	2023 Apr 26	P200	1.76	15	$g + r$
J1302+1650	2022 Jul 4	P200	1.40	10	$g + r$
	2023 Mar 26	P200	4.05	10	$g + r$
	2023 Mar 27	P200	5.90	10	$g + r$
J1650+1443	2022 Jul 2	P200	0.98	10	$g + r$
	2022 Aug 24	P200	2.93	10	$g + r$
J1944+4557	2022 Mar 23	P200	1.26	10	$g + r$
	2022 Apr 29	McD	2.58	15	BG40
	2022 Sep 29	P200	1.54	10	$g + r$

Note. In the Facility column, PTO indicates the Perkins 1.8 m telescope, P200 indicates the Palomar Hale 200 in telescope, and McD indicates the McDonald 2.1 m Otto Struve telescope, using the PRISM, CHIMERA, and ProEM instruments, respectively.

standard calibration frames taken each night to bias and flat-field correct our images. We performed differential circular aperture photometry and light curve extraction using the ULTRACAM pipeline (Dhillon et al. 2007). Optimal extractions (Naylor 1998) were performed using a variable aperture radius set to 1.5 times the full-width half-maximum (FWHM) of each image, measured from the reference star. We clipped 5σ outliers from the light curves, and performed barycentric corrections to the GPS timestamps of our images using the Astropy (Astropy Collaboration et al. 2018) Python package.

McDonald/ProEM. We carried out time series photometry for one object at McDonald Observatory using the Princeton Instruments ProEM frame-transfer CCD attached to the 2.1 m Otto Struve Telescope. We used a Newport Optics blue-bandpass BG40 filter (3500–6500 Å) and an exposure time of 15 s. Using standard calibration frames taken during each night of observations, we dark and flat-field corrected our images using the IRAF reduction suite. We then performed differential circular aperture photometry using the IRAF ccd_hsp package (Kanaan et al. 2002) with aperture radii ranging from 2 to 10 pixels in half-pixel steps. Local sky subtraction was performed for each object using an annulus centered on each aperture. We generated divided light curves using the PHOT2LC reduction software (Vanderbosch 2022), selecting the aperture size that maximized the signal-to-noise (S/N) of the light curve. We clipped 5σ outliers and again used Astropy to perform barycentric corrections to the mid-exposure GPS time stamps of our images.

Table 4
Spectroscopic Observations

Name (WD)	UT Date	Facility	t_{exp}(Blue) (s)	t_{exp}(Red) (s)	Seeing ($''$)	Airmass	Aper. ($''$)	λ (Å)	$\lambda_{dichroic}$ (Å)	R ($\lambda/\Delta\lambda$)
J0923+7326	2021 Dec 29	Keck/LRIS	1×600	1×600	1.1	1.68	1.0	3140–10290	5644	1560(B)/970(R)
J1013–0427	2022 Nov 16	Keck/LRIS	1×600	1×600	1.1	1.21	1.0	3140–10280	5644	1560(B)/970(R)
	2022 Nov 23	Keck/LRIS	1×1200	1×1200	1.0	1.51	1.0	3140–8820	5644	1560(B)/1560(R)
	2023 Jan 15	Keck/LRIS	1×900	1×900	1.4	1.33	1.0	3140–9320	6669	1580(B)/4850(R)
	2023 Feb 15	Keck/ESI	2×1160	$\cdots$	1.1	1.13	0.75	4000–9200	$\cdots$	5400
	2023 May 23	Keck/LRIS	11×610	11×600	1.2	1.51	1.0	3140–8780	5644	1570(B)/1520(R)
J1237+5937	2022 Jun 25	P200/DBSP	2×900	2×900	1.6	1.33	1.5	3200–10800	5588	1060(B)/960(R)
	2023 Jan 15	Keck/LRIS	1×1200	2×575	0.9	1.37	1.0	3140–8780	5643	1100(B)/1600(R)
J1302+1650	2022 Jun 25	P200/DBSP	1×1200	1×1200	1.6	1.47	1.5	3200–10800	5588	1060(B)/960(R)
	2022 Jul 4	Keck/LRIS	1×900	$\cdots$	1.5	1.55	1.0	3140–5644	$\cdots$	1550(B)
	2023 Apr 20	Keck/LRIS	1×1200	1×1200	0.9	1.00	1.0	3060–10240	5666	780(B)/1000(R)
J1650+1443	2022 Jul 3	P200/DBSP	1×1200	1×1200	2.1	1.07	1.5	3200–10940	5754	1060(B)/960(R)
	2022 Jul 4	Keck/LRIS	1×600	1×600	1.4	1.13	1.0	3140–10280	5645	1550(B)/1000(R)
J1944+4557	2022 May 6	P200/DBSP	2×600	2×600	1.2	1.07	1.5	3200–10800	5627	1060(B)/960(R)
	2022 Jul 4	Keck/LRIS	3×600	3×600	1.5	1.14	1.0	3140–10280	5644	1550(B)/930(R)
	2022 Nov 21	P200/DBSP	3×900	3×900	1.4	1.33	1.5	3200–10990	5773	1060(B)/960(R)
J2241+3712	2022 Aug 25	P200/DBSP	1×1200	1×1200	1.0	1.01	1.0	3200–10900	5717	1600(B)/1400(R)
	2022 Aug 26	Keck/LRIS	1×600	1×600	0.9	1.06	1.0	3140–10280	5643	1590(B)/980(R)

Note. For WD J1302+1650, only a blue-arm exposure was acquired with Keck/LRIS on 2022 July 4, hence the shorter wavelength coverage. Also, for the observation of WD J1013–0427 on 2023 February 15, the ESI spectrograph was used which does not have a separate blue or red arm.

Perkins/PRISM. We observed one object, WD J1013–0427, on 2022 December 25 at the 1.8 m Perkins Telescope Observatory (PTO) using the Perkins Re-Imaging SysteM (PRISM; Janes et al. 2004) mounted at Cassegrain focus. PRISM employs an e2v CCD230-42-0-E10 back-illuminated CCD which covers a 13.3 field of view at a plate scale of $0''.39$ per pixel. We used the blue-bandpass, red-cutoff BG40 filter with integration times of 40 s. PRISM is liquid nitrogen-cooled with negligible dark current. We bias subtract and flat field our images using standard IRAF routines. We used the CCD_HSP IRAF routine (Kanaan et al. 2002) to perform aperture photometry over circular apertures ranging in radius from 0.5 to 10.0 pixels. We again use PHOT2LC to extract the optimal light curve.

3.2. Low-resolution Spectroscopy

Palomar/DBSP. None of our targets had any prior spectroscopic observations, so we first obtained identification spectra for most objects using the Double Spectrograph (DBSP; Oke & Gunn 1982) attached at Cassegrain focus of the Palomar 200-in Hale Telescope. For all DBSP observations, we used the D55 dichroic, the 600 line mm^{-1} grating for the blue arm blazed at 3780 Å, and the 316 line mm^{-1} grating for the red arm blazed at 7150 Å. We used grating angles of $27°17'$ and $24°38'$ for the blue and red sides, respectively. With these setups and the $1''.5$ longslit we achieve resolving powers of $R \approx 1060$ in the blue arm and $R \approx 960$ in the red arm. These increase to $R = 1600$ and $R = 1400$, respectively, when using the $1''.0$ longslit. These setups provide continuous spectral coverage across 2900–10

800 Å, with the division between blue and red arms (λ_{BR}) typically occurring around 5650 Å (see Table 4 for a more detailed summary of individual observations). We reduced the spectra using the DBSP_DRP reduction pipeline (Roberson et al. 2021; Mandigo-Stoba et al. 2022a, 2022b), which is built on the PypeIt python package (Prochaska et al. 2020b, 2020a). The standard stars BD+28 4211, BD+33 2642, or Feige 34 were used for flux calibration.

Keck/LRIS. To identify or improve on the S/N of some objects, we obtained spectra using the Low Resolution Imaging Spectrograph (LRIS, Oke et al. 1995; Rockosi et al. 2010) on the Keck-I 10 m telescope at Mauna Kea Observatory. For all observations we used the $1''.0$ longslit and the D560 dichroic. On the blue arm we used the 600 line mm^{-1} grism blazed at 4000 Å, and on the red arm we used either the 400 line mm^{-1} grating blazed at 8500 Å or the 600 line mm^{-1} grating blazed at 7500 Å. With these setups we achieve resolving powers of $R = 1100$ on the blue side, and either $R = 1100$ or $R = 1500$ on the red side for the 400 and 600 line mm^{-1} gratings, respectively. These setups provide continuous spectral coverage of either 3140–10280 Å or 3140–8820 Å depending on whether the 400 and 600 line mm^{-1} grating was used, with $\lambda_{BR} = 5644$ Å in both cases. For the observations of WD J1302+1650 on 2022 July 4, we only obtained an exposure in the blue arm, so the spectral coverage is limited to 3140–5644 Å. We reduced the spectra using the LRIS automated reduction pipeline (LPipe; Perley 2019). The standard stars BD+28 4211, BD+33 2642, or G191–B2B were used for flux calibration.

Keck/ESI. To obtain higher-resolution observations of one object, WD J1013–0427, we used the Keck Echellete Spectrograph and Imager (ESI; Sheinis et al. 2002). Using ESI in echelle mode with the 0."75 slit, on 2023 February 15 we acquired two 1160 s exposures with a spectral resolution of $R = 5400$. We extracted and wavelength calibrated 1D spectra for each echelle order using the MAKEE software suite.

4. Results

We visually inspected the ZTF light curves of all the objects in the top 1%, along with their atmospheric parameters: the effective temperature, $T_{\rm eff}$ and $\log(g\,[{\rm cm\,s^{-2}}])$ as inferred from H-dominated atmosphere fits to their Gaia photometry. We searched for objects with irregular variability, without any significant Lomb–Scargle period. This eliminates the possibility of the objects being binary systems, rotational variables or pulsators. Concerning the latter, we also gave preference to objects lying outside the white dwarf pulsational instability strips. Additionally, we also checked the position of the object in the η–S_P space and gave preference to objects lying in the third quadrant (see previous discussion in Section 2.6). Following this, we obtained follow-up optical spectroscopic observations of seven highly promising candidates, primarily using DBSP and LRIS. The ZTF light curves are presented in Figure 3, the position of these objects in the Gaia color–magnitude diagram (CMD), along with the other variables, are presented in Figure 4, and the best quality spectra are presented in Figure 5. Out of them, six objects showed prominent metal absorption lines (the most prominent being the Ca II K 3933 Å line), indicative of metal pollution. The spectra also eliminate the possibility of the objects being any symbiotic systems or CVs, as no emission lines typical of these systems are observed. The metal pollution along with the high photometric variability strongly indicates the transiting debris nature of these white dwarfs. We present these six objects as new candidate systems (Section 4.1). The remaining object shows prominent helium emission lines, typical of an AM Canis Venaticorum (AM CVn) system. The ZTF light curve shows a long-duration outburst, making this a rare type of system. We present this as a serendipitous additional discovery (Section 4.2).

4.1. New Candidates for Transiting Debris

For all the candidates, we fitted the LRIS spectra using the Koester white dwarf atmosphere models (Koester 2010) to obtain white dwarf atmospheric parameters: $T_{\rm eff}$, $\log(g)$. To achieve this, we performed least squares fits of the models, against the spectra as well as available photometric fluxes (Gaia DR3, SDSS, Pan-STARRS, and Galex).[20] For the

---

[20] In the case of WD J1302+1650, the Gaia photometry is significantly offset below the SDSS and Pan-STARRS photometry, potentially due to increased obscuration from the transiting debris for these observations. Therefore for this object, we excluded the Gaia photometry from our fitting.
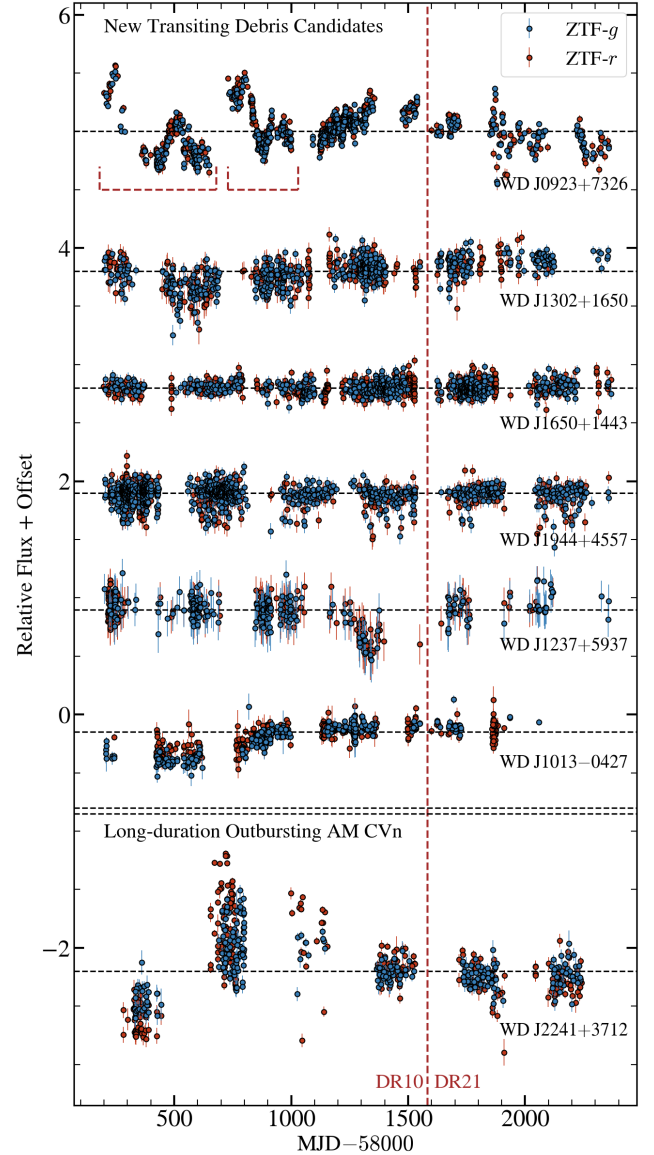
Figure 3. The ZTF light curves for the new transiting debris candidates and the long-duration outbursting AM CVn. We present the light curves from a more recent ZTF data release (DR21, span: 2018 March to 2024 February), but we mark the end of DR10, which represents the portion of the light curves that has been used for the sample selection.

spectral part of the fit, the models were normalized against the data by fitting a spline against the ratio of spectrum and model. Models were convolved to the instrumental resolution, and the radial velocity (RV) included as a further free-parameter.[21] For the photometric part of the fit, the Gaia parallax is used as a prior in order to fold in its uncertainty into the estimate of the surface gravity (where the scaling of the spectral model against

---

[21] Flexure and other instrumental effects render our RVs unreliable, so we do not report them here. Nearly all of our inferences remain unaffected by this.
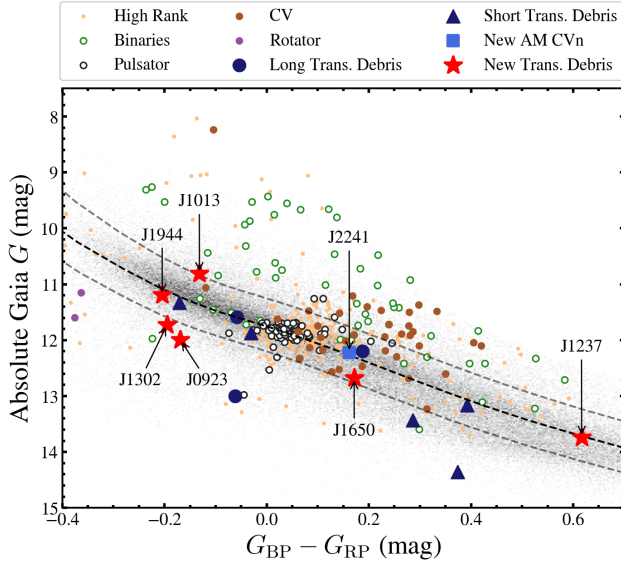
Figure 4. Position of the white dwarfs in Gaia CMD. The same presentation scheme as in Figure 2 is followed for the objects. For reference, we mark the theoretical cooling track of H-atmosphere WD (Bédard et al. 2020) with three masses: the black dashed line for that of a $0.6M_\odot$ white dwarf, and the upper and lower gray lines for $0.4M_\odot$ and $0.8M_\odot$ WD, respectively.

the photometry used the mass–radius relations of Bédard et al. 2020). We also included interstellar reddening (E_{B-V}) as a free-parameter, using the extinction model of Gordon et al. (2023) and $R_V = A_V/E_{B-V}$ fixed to 3.1.

Apart from H, and He, we include the following metals in the fitting process: Mg, Al, Si, Ca, Fe, and Ni. However, in most objects, only a subset of these metals were detected in our optical spectra, and so the unseen elements were scaled to bulk Earth abundance ratios (Allègre et al. 2001; Zuckerman et al. 2010), typically relative to Ca, which is detected in all objects. The inclusion of these unobserved elements is still required to consider opacities outside of the optical, such as the Mg II h+k resonance lines in the near-ultraviolet. For WD J1013–0427 and WD J1302+1650, which have helium-dominated atmospheres,[22] H was also included as a free-parameter to measure their abundances of trace hydrogen. For WD J1237+5937 and WD J1650+1443, which have H-dominated atmospheres, it was necessary to account for 3D effects which are not accounted for in our 1D atmospheric models. Therefore for the spectroscopic parts of their fits, we calculated separate models, inverting the 1D to 3D corrections given by Tremblay et al. (2013). WD J1944+4557 is hot enough that its atmosphere is fully radiative and the 1D to 3D corrections are negligible. Table 5 summarizes the derived atmospheric parameters and elemental abundances.
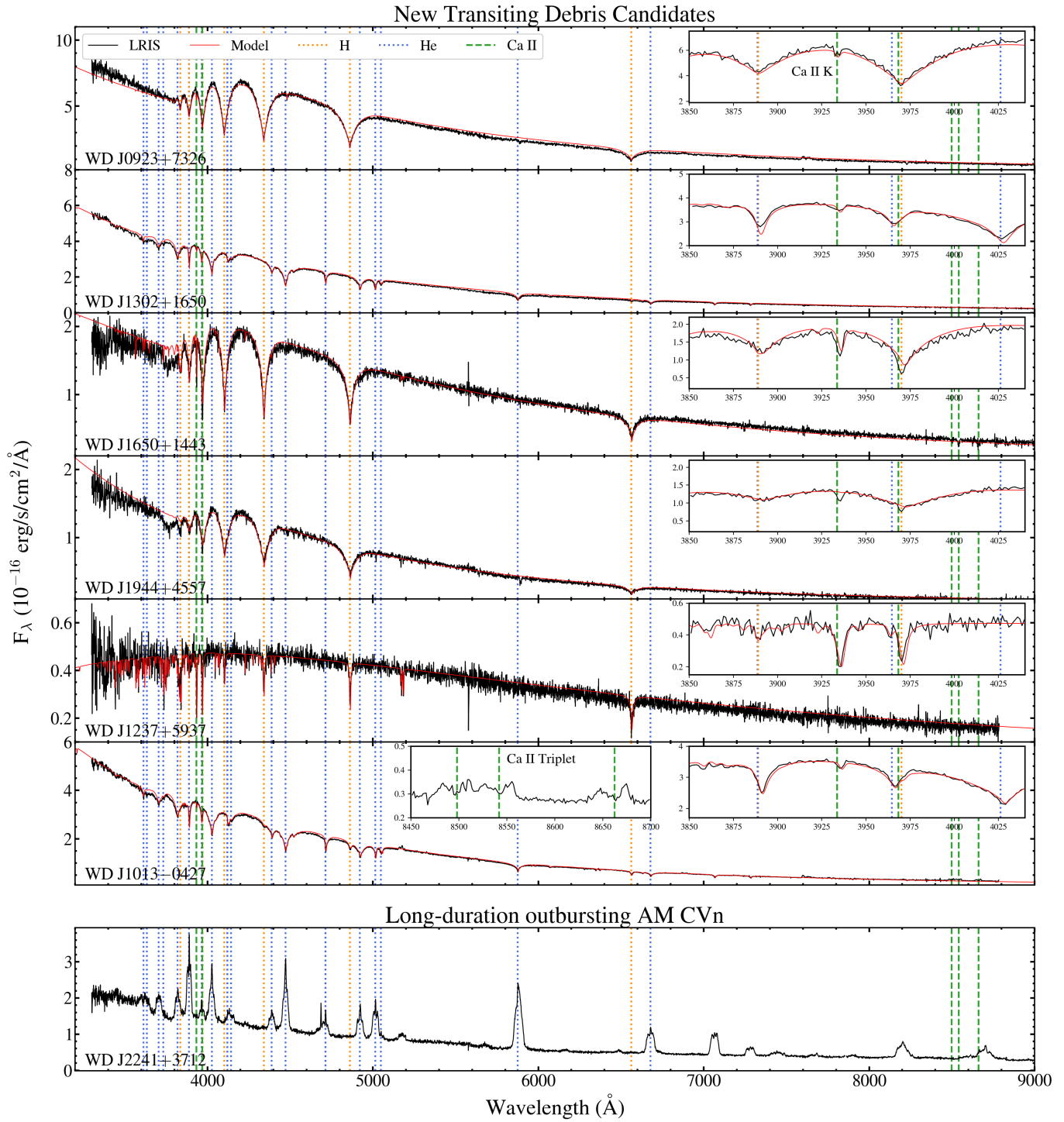
For all the candidates, we calculate the metal accretion rates from the inferred metal abundances. We assume a steady state (accretion rate equals the surface convective diffusion rate) for each metal individually. For a given metal Z, we calculate the latter as $M_Z^{\mathrm{cvz}}/t_Z^{\mathrm{diff}}$ where M_Z^{cvz} is the mass of the metal in the convection zone of the white dwarf and t_Z^{diff} is the diffusion timescale. We further use the relation: $M_Z^{\mathrm{cvz}} = M_{\mathrm{WD}} \cdot 10^{q_{\mathrm{cvz}}} \cdot 10^{[Z/\mathrm{H(e)}]} \cdot A_Z/A_{\mathrm{H(e)}}$ where q_{cvz} is the logarithm of the convection zone mass fraction and A denotes the atomic mass [H(e) denotes either H or He for respective white dwarf atmospheres], and $[Z/\mathrm{H(e)}]$ is the metal abundance as derived from the spectrum.

To obtain the quantities q_{cvz} and t_Z^{diff}, we use the publicly available grids of white dwarf envelop parameters from the work of Koester et al. (2020). We use the (updated) model grid tables provided on the author's website[23] and perform a linear interpolation to the stellar parameters of our objects. We use both the tables with no overshoot ("0.0Hp") and overshoot of one pressure scale height ("1.0Hp") for accretion rate calculations and report the mean. The difference in the resultant accretion rates from the two cases, however, is never more than a few percent and almost always smaller than the uncertainty in the abundance measurements. We note here that two of our objects, WD J1302+1650 and WD J1013–0427, are DBAZs (containing both H and He in the atmosphere, along with metals). The inferred stellar parameters, however, are much beyond the DBAZ envelop grids available. Thus, for these two objects, we use the tables for a He-dominated atmosphere. A similar situation also arises with a DA white dwarf in the sample, WD J1944+4557. The inferred temperature for this object is marginally beyond the highest temperature in the envelop grid (20,250 K). We proceed by simply using the value corresponding to this limiting temperature. For a T_{eff} and $\log(g)$, we use the evolutionary models of Bédard et al. (2020) to obtain the corresponding M_{WD}.

We obtain the accretion rates of all the metals included in the models individually using the above methodology. This includes those that are not directly detected in the spectra, but were estimated from the bulk Earth-abundance ratios relative to Ca. We then add all the accretion rates to get an estimate of the total accretion rate. The results are provided in Table 5. There might, however, be other metals not included in the models but still contributing significantly to the mass accretion rate (oxygen, for example). Thus, we also provide the total rate estimates using the Mg and Ca accretion rates scaled up by their respective mean bulk Earth-abundances (15.8% and 1.67% respectively, see Zuckerman et al. 2010; Xu et al. 2019a). Owing to the uncertainty in the abundance estimation of certain elements, we do not report a statistical error.

---

[22] All the DA and DB objects in the paper have H-dominated and He-dominated atmospheres, respectively. Thus, the spectral type and atmospheric type have sometimes been used interchangeably in the texts that follow.

[23] https://www1.astrophysik.uni-kiel.de/ koester/astrophysics/astrophysics.html

Figure 5. The spectra of the six new transiting debris candidates (top six panels) and the AM CVn (bottom panel). Out of the several observations, only the best signal-to-noise spectrum is shown here. For each of the transiting debris candidates, we also over-plot the best-fit white dwarf atmosphere model. We also provide close-in view around the Ca II H and K lines as insets. For WD J1013–0427, we provide an additional inset showing the Ca II triplet emission lines.

Table 5
Summary of the New Transiting Debris Candidates

WD	J0923+7326	J1302+1650	J1650+1443	J1944+4557	J1237+5937	J1013−0427
Spectral Type	DAZ	DBAZ	DAZ	DAZ	DAZ	DBAZ
GAIA PARAMETERS						
Gaia DR3	1121123185951605632	3937407901354145536	4461588765542688768	2080201713998110336	1578454838386128384	3780094656734582528
R.A. (deg)	140.96429	195.57365	252.70835	296.13298	189.47594	153.27634
Decl. (deg)	+73.43995	+16.83565	+14.72290	+45.96471	+59.62424	−04.45820
Parallax (mas)	5.6371 ± 0.1033	3.2169 ± 0.2643	5.9503 ± 0.1709	2.3201 ± 0.2206	5.2751 ± 0.5109	3.2469 ± 0.1913
G (mag)	18.24	19.18	18.80	19.36	20.12	18.25
SPECTRAL-FIT PARAMETERS[a]						
T_{eff} (K)	13710 ± 165	18400 ± 220	10250 ± 120	20790 ± 250	6480 ± 75	21900 ± 50
$\log(g\,[\mathrm{cm\,s^{-2}}])$	8.25 ± 0.04	8.19 ± 0.04	8.22 ± 0.04	8.27 ± 0.05	7.79 ± 0.12	8.06 ± 0.04
Mass ($M_\odot$)	0.76 ± 0.03	0.71 ± 0.03	0.74 ± 0.03	0.79 ± 0.03	0.47 ± 0.06	0.64 ± 0.03
Parallax (mas)	5.09 ± 0.09	2.73 ± 0.03	5.45 ± 0.10	2.50 ± 0.09	4.61 ± 0.29	3.16 ± 0.02
E_{B-V}	0.005 ± 0.013	0.029 ± 0.008	0.024 ± 0.009	0.062 ± 0.012	−0.007 ± 0.020	0.052 ± 0.004
ABUNDANCE RATIOS[b]						
H	Atm.	−4.73 ± 0.04	Atm.	Atm.	Atm.	−2.52 ± 0.01
He	⋯	Atm.	⋯	⋯	⋯	Atm.
Mg	−4.99 ± 0.06	⋯	−5.24 ± 0.08	⋯	−6.24 ± 0.09	−4.05 ± 0.04
Al	⋯	⋯	⋯	⋯	−7.79 ± 0.24	⋯
Si	⋯	⋯	⋯	⋯	⋯	−4.10 ± 0.01
Ca	−6.13 ± 0.08	−6.89 ± 0.03	−5.83 ± 0.07	⋯	−7.95 ± 0.09	−5.37 ± 0.04
Fe	⋯	⋯	⋯	⋯	−6.76 ± 0.11	⋯
ACCRETION RATES[c]						
$\log(\dot{M}\,[\mathrm{g\,s^{-1}}])$	8.78	9.66	10.15	⋯	9.13	9.82
$\log(6.33 \times \dot{M}_{Mg})$	8.67	⋯	9.77	⋯	9.40	9.93
$\log(60 \times \dot{M}_{Ca})$	8.94	9.84	10.42	⋯	9.00	9.89

Notes.

[a] A minimum systematic error of 1.2% in T_{eff} and 0.04 dex in $\log(g)$ are provided. The corresponding masses were obtained from Bédard et al. (2020).

[b] The elemental abundances are with respect to the dominant atmospheric element (designated as "Atm" in the table) and are in the units of [Z/H(e)]. The inference for WD J1944+4557 is uncertain (see text). The statistical uncertainties in the estimated accretion rates are expected to be of the same order as those of the abundances. Note, however, that the "true" uncertainties can be larger as differences due to modeling systematics for both the abundances and accretion rates may surpass statistical uncertainties.

[c] We provide three estimates of the total accretion rates. First row: sum of accretion rates of all elements considered in the model (both the detected and the non-detected, the latter being fixed assuming bulk Earth abundances). Second and Third rows: Scaling up the detected Mg and Ca accretion rates assuming bulk Earth abundance of 15.8% and 1.67%, respectively.

In the rest of the section, we briefly discuss the properties of the transiting debris candidates individually and perform preliminary analyses. We present the spectral energy distributions (SEDs) of these objects separately in Figure 17 under Appendix B.

4.1.1. WD J0923+7326

The object was identified as a white dwarf candidate based on Gaia DR2 astrometry and photometry (Jiménez-Esteban et al. 2018; Gentile Fusillo et al. 2019) and re-appears in the eDR3-based catalog of Gentile Fusillo et al. (2021b) (on which this work is based on). The ZTF light curve of this object shows extreme variability. It clearly shows a long-timescale variability along with short-timescale jitter. This makes this object one of the most variable objects in our top 1%. It was also classified as a variable in Guidry et al. (2021) and was initially suspected to be a CV or similar accreting system (due to its erratic light curve). However, follow-up optical spectroscopy ruled out this scenario, showing no emission lines. Furthermore, it shows clear signatures of metal pollution, strengthening its candidacy as a transiting debris object. Due to its long-timescale trend, the object has a very low η value and a mild negative S_P. Overall, the object lies in the third quadrant of the η–S_P space, along with the other debris objects.

The atmospheric properties derived from Gaia eDR3 photometry are $T_{\rm eff} = 16,700 \pm 3700$ K and $M = 0.94 \pm 0.15\,M_\odot$. Using the Keck LRIS spectrum from 2022 July 4 and SDSS, Pan-STARRS1, and Gaia DR3 photometry, we derive atmospheric parameters of $T_{\rm eff} = 13,710 \pm 165$ K and $M = 0.76 \pm 0.03\,M_\odot$. The revised $T_{\rm eff}$ is broadly consistent with the Gaia inference, but the revised mass is significantly lower. We suspect that the higher mass estimation with Gaia photometry resulted from it being underluminous in the CMD (see Figure 4), possibly due to debris occultation.

We also note here that the parallax inferred from the spectral fit (5.09 $\pm$ 0.09 mas) is lower than the Gaia parallax (5.64 $\pm$ 0.10 mas) by about 4σ. This may result from the fact that the object is under luminous, thus requiring a larger distance to match the model flux to that observed. A second possibility is that there is a gray component to the extinction from the circumstellar material, violating the assumption of $R_V = 3.1$. Yet another, but less likely, reason is that the fit is not optimal. Nevertheless, for the purpose of this paper, we proceed with these inferences.

The ZTF light curve shows high amplitude variability over timescales of several years. We notice a qualitative similarity between the morphology of the light curves from the first two seasons (marked in Figure 3). If this recurrence is a true feature, this may hint at a orbital period of ~500 days. However, the light curve changes soon after the second season, preventing any further study of the possible long period. A

long-timescale modulation, however, persists. Dips on short timescales are confirmed with the high-speed photometric follow-up, as presented in Figure 6.

To investigate the activity of this object prior to the start of ZTF, we queried its light curve from the Asteroid Terestrial-impact Last Alarm System (ATLAS) survey.[24] The light curve indicates a prominent long-timescale brightening just prior to the ZTF data by a factor of $\gtrsim$1.5. A brightening is unusual for this class of systems. However, an inspection of the ATLAS images and light curves of neighboring field stars indicate possibility of bad photometry (possibly through blending with a star 0.7 mag brighter in Gaia G 9″.6 away and another star 8″.1, albeit 0.6 mag fainter). This is supported by the rejection of a significant portion of the data with the application of reasonable quality cuts.[25] Additionally, the forced photometry on the difference images does not show the said brightening. Thus, due to these uncertainties, we do not show the data or discuss this feature further.

The spectrum shows absorption features of Ca and Mg, with inferred respective abundances of [Ca/H] = -6.13 ± 0.08, and [Mg/H] = -4.99 ± 0.06. The estimated total accretion rate is $\log(\dot{M}\,[{\rm g\ s^{-1}}]) \simeq 8.78$. We compare this to the corresponding range of values for metal-polluted white dwarfs reported in Table 6 in Xu et al. (2019a). The values for WD J0923+7326 are mostly consistent with the distribution for H-dominated white dwarfs, but more consistent with those of white dwarfs with detected dust disks through infrared excess (henceforth, the "dusty scenario"). The SED suggests a possible infrared excess in the Wide-field Infrared Survey Telescope (WISE) W1 and W2 data (see Figure 17, he available W3 and W4 fluxes are upper limits thus excluded) however closer inspection renders them unreliable, owing to severe blending with the same two nearby stars as discussed in context of ATLAS.

4.1.2. WD J1302+1650

This object was first identified as a DB white dwarf using an SDSS spectrum acquired on 2007 February 18 (Kleinman et al. 2013), and later as a DBA with [H/He] = -4.4 ± 0.3 through further analysis of the same SDSS spectrum (Genest-Beaulieu & Bergeron 2019). A second SDSS spectrum was also acquired on 2012 April 20 and released during DR16. As a relatively faint source (G = 19.2 mag), the signal-to-noise ratios (SNRs) of the two SDSS spectra were too low to identify any metallic absorption features, with median SNRs of 8.8 and 12.2 for the first and second spectra, respectively. We obtained

---

[24] We queried the science-image forced photometry data from the online service at https://fallingstar-data.com/forcedphot/ (Shingles et al. 2021).
[25] We reject all data where err≠0, and the signal-to-noise is <5. Furthermore, to ensure good photometry, we only consider data where the PSF-fit reduced χ^2chi/N is between 0.5 and 2. We note here that we use these same quality cuts with the data provided for WD J1013–0427 discussed in Sections 4.1.6 and 5.1.
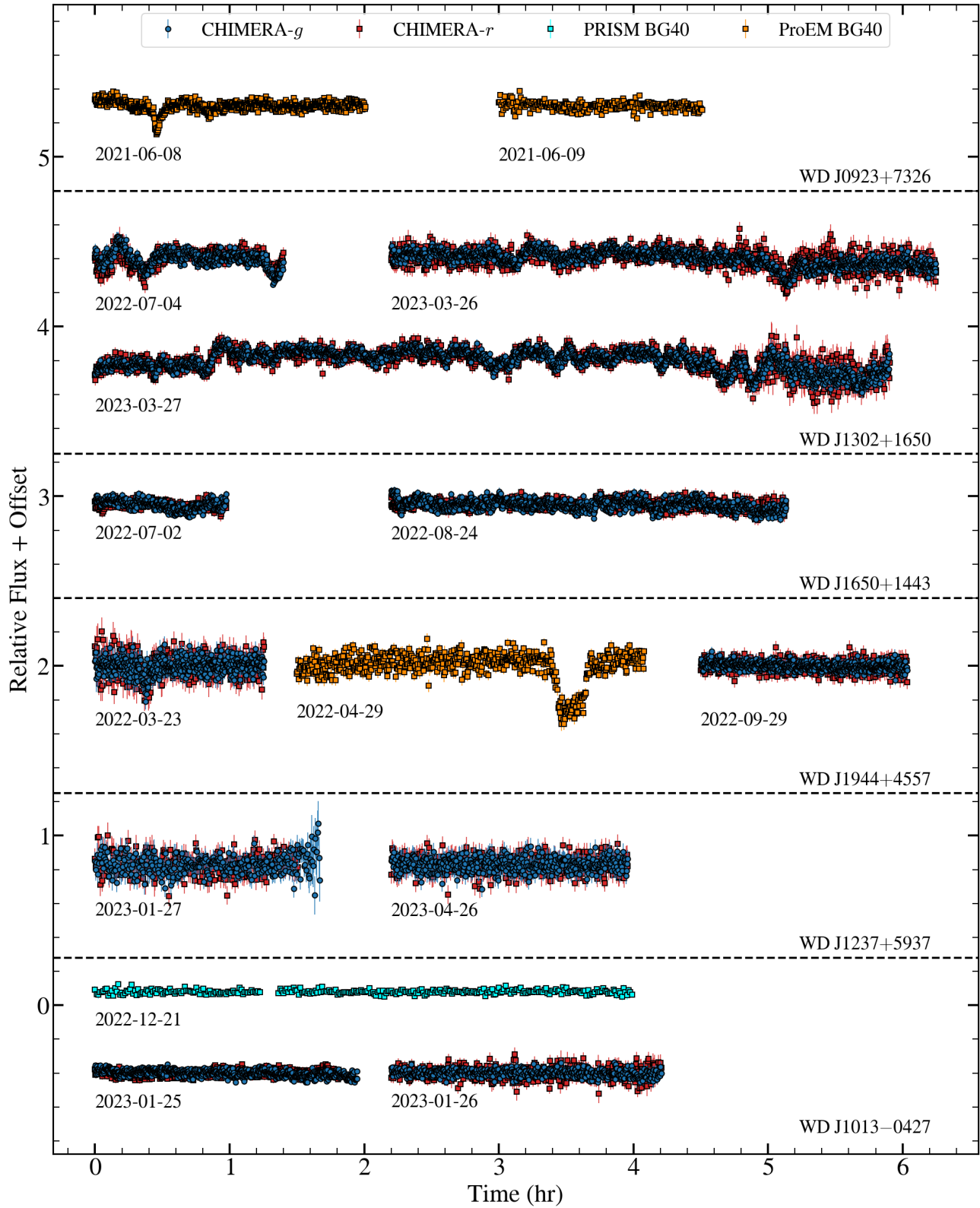
Figure 6. The follow-up high-speed photometric light curves for the five new transiting debris candidates. Three of the six candidates: WD J0923+7326, WD J1302 +1650, and WD J1944+4557 show clear short timescale dips and transits, strongly suggestive of ongoing debris activity. The other three objects do not show significant activity in these light curves.

higher SNR spectra first using DBSP and then LRIS, both of which show a clear detection of Ca II K 3933 Å absorption feature while also confirming the presence of H-α absorption, modifying the spectral type of WD J1302+1650 once again to DBAZ.

The analysis by Genest-Beaulieu & Bergeron (2019) of the early SDSS spectrum and *ugriz* photometry plus Gaia DR2 astrometry provides photometric ($T_{\rm eff}$ = 20,760 ± 2280 K, M = 0.93 ± 0.10$M_\odot$) and spectroscopic ($T_{\rm eff}$ = 19,520 ± 880 K and M = 0.81 ± 0.09$M_\odot$) atmospheric parameters. These values are in agreement with the mixed H/He-atmosphere parameters based on Gaia eDR3 photometry and astrometry alone (Gentile Fusillo et al. 2021a), where $T_{\rm eff}$ = 17,700 ± 7100 K and M = 0.91 ± 0.36$M_\odot$.

We used our own Keck LRIS spectrum for this object taken on 2023 April 20, along with archival SDSS *ugriz* and Pan-STARRS1 *grizy* photometry, to obtain the updated atmospheric parameters as $T_{\rm eff}$ = 18,400 ± 220 K, M = 0.71 ± 0.03$M_\odot$. These values are consistent with the Gaia eDR3 and SDSS estimates. The previous mass estimates have a higher value than the revised estimate likely due to the object being under-luminous in CMD owing to debris transits (Similar to WD J0923+7326, see Figure 4). Alongside this, we obtain a [H/He] abundance of −4.73 ± 0.04, consistent with that inferred in Genest-Beaulieu & Bergeron (2019) using the SDSS spectrum.

The ZTF light curve shows a long-lasting dip feature at around MJD of 58700. This feature is well-resolved in ZTF cadence, which places the object well within the third quadrant of the η–S_P space. On top of this long-timescale trend, the scatter in the data points indicates additional variability on shorter timescales. This is substantiated by the results from the high-speed follow-up photometry with CHIMERA (see Figure 6). During all three nights of observation, this object shows nearly continuous and irregular variability with the largest peak-to-peak variations exceeding 20%. The CHIMERA light curves of this object bear a strong resemblance to the relentless transit activity observed in WD 1054–226 (Farihi et al. 2022). The long-timescale trend can be a result of variation of transit activity, with higher activity skewing the light curve to lower flux values. Such behavior has been reported in several other transiting debris systems (WD J0328–1219, and others, see Aungwerojwit et al. 2024).

We model the long-timescale dip in the ZTF light curve using the asymmetric hyperbolic secant function (AHS, as in Rappaport et al. 2016; Xu et al. 2019b)

$$f(t) = f_0 \left(1 - \frac{2f}{e^{\frac{t-t_0}{\phi_1}} + e^{-\frac{t-t_0}{\phi_2}}} \right), \qquad (8)$$

where f_0 is the out-of-transit flux (in reference flux unit, this is unity), ϕ_1 and ϕ_2 are the ingress and egress timescales, and f
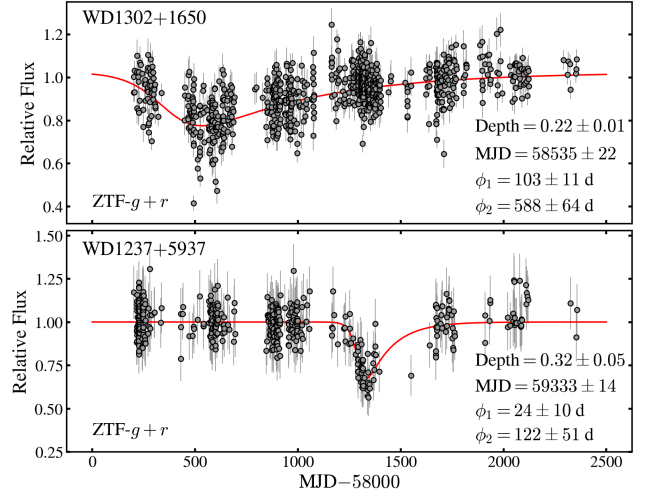
Figure 7. The AHS (Equation (8)) fit to the ZTF light curves of WD J1302 +1650 and WD J1237+5937. The inferred parameters, namely the transit depth, epoch of transit, and the ingress and egress durations (in days) have been provided in the figure.

and t_0 parameterize the depth and the epoch of the transit.[26] No color-dependence of the transit was seen, thus we use the combined (in relative flux units) ZTF-*g* and *r* data to fit the function. The result, along with the inferred properties are shown in Figure 7 (top panel). The inferred (median) depth is ≈20% (though there are data points indicating up 60% drop in flux). The inferred egress time is significantly longer than the ingress time. This is expected in scenarios of collisions between larger debris in the dust disk, leading to the production of dust/debris, which condenses back on longer timescales. Such occurrences can lead to larger obscuration or elevated debris activities, perceived as the long-timescale dip.

The LRIS spectrum shows photospheric absorption features of Ca, for which we obtain an abundance of [Ca/He] = −6.89 ± 0.03 from the spectral fit. We compare this to the corresponding range of values for metal-polluted white dwarfs reported in Table 6 in Xu et al. (2019a). The abundance is broadly consistent with those reported for DBs, more so with the dusty scenario. The estimated total accretion rate of $\log(\dot{M})$ ≃ 9.66 ± 0.2 is consistent with the distribution for He-dominated white dwarfs reported in (Xu et al. 2019a).

4.1.3. WD J1650+1443

To date, this object has only been considered a candidate white dwarf based on Gaia DR2 and eDR3 photometry and astrometry (Gentile Fusillo et al. 2019; Gentile Fusillo et al. 2021a). Both the

---

[26] Note that f and t_0 do not exactly correspond to the depth and epoch of transit, and are shifted from the true values (see Rappaport et al. 2016). We use the model fit to calculate the true depth and transit epoch. However, we simply use the model-fit errors of f and t_0, as the errors of the "true" values, as they are not expected to differ significantly.

DBSP and LRIS spectra, with prominent Balmer and Ca II K absorption lines, suggest that it is a DAZ white dwarf. The atmospheric properties derived from Gaia eDR3 photometry are $T_{\rm eff} = 10{,}260 \pm 630$ K and $M = 0.80 \pm 0.10\,M_\odot$. Using the Keck LRIS spectrum from 2022 July 4 and SDSS, Pan-STARRS1, and Gaia DR3 photometry, we derive atmospheric parameters following the same methodology described in Section 4.1.2 of $T_{\rm eff} = 10{,}250 \pm 120$ K and $M = 0.74 \pm 0.03\,M_\odot$, consistent with the Gaia inferences. Like WD J0923 +7326, the model-inferred parallax (5.37 ± 0.11 mas) is lower than the Gaia parallax of 5.95 ± 0.17 mas (by about 3σ). We suspect the same possible reasons as discussed for WD J0923 +7326, but proceed with these inferences.

The spectrum shows absorption features of Ca and Mg, with inferred respective abundances of [Ca/H] = -5.83 ± 0.07, and [Mg/H] = -5.24 ± 0.08. The estimated total accretion rate is $\log(\dot{M}) \simeq 9.98$. The Ca and Mg abundances are consistent with the distributions for DAs reported in Xu et al. (2019a). The estimated accretion rate, however, is significantly (about an order of magnitude) higher than the usual distribution for H-dominated white dwarfs. This can indicate a highly active accretion state in the system or overestimation of the metal abundances. For further discussion, see Section 6.

The light curves for this object show only low amplitude variability. The ZTF light curve shows "jittering" variability, with a small flux amplitude ($\approx$10% in flux) around a median. Small amplitude variability ($\approx$5% in flux) is also witnessed in the CHIMERA light curves. We note here that the amplitude may appear too small to confidently claim that the object is variable. However, its position in the top 1% in terms of the R metric (with a metric value of 13.38) strongly suggests its variability. We checked that the 5σ clipped range of R of objects having Gaia G magnitude within ± 0.5 of WD J1650+1443 is 0.4 ± 2.3 which is much lower. However, closer inspection shows that Gaia metric, V_G, contributes to most of its variability with $V_G = 11.5$. The ZTF metric of $V_{\rm ZTF} = 1.9$, in fact, does not indicate strong variability when compared to the other objects of similar magnitude. This may indicate that the object was variable during the Gaia observations, but is no more variable in the recent past. This is indeed possible, given the long quiescent phases observed in many transiting debris systems (Aungwerojwit et al. 2024, this work), which follows a previous period of high activity. Further long-term photometric monitoring of the object is needed to detect any ongoing signature of debris activity. Another possibility is bad Gaia photometry, making the high V_G value an artifact. Unfortunately, the Gaia epochal photometric data is not available to investigate this possibility.

4.1.4. WD J1944+4557

Similar to the previous candidate, this object has only appeared as a candidate white dwarf in Gaia DR2 and eDR3 catalogs (Gentile Fusillo et al. 2019; Gentile Fusillo et al.

2021b). The ZTF light curve for this object shows significant variability with sporadic but prominent dips. This object, too, finds itself in the third quadrant in the η–S_P space. Both the DBSP and LRIS spectra, with prominent Balmer and Ca II K absorption lines, suggest that it is a DAZ white dwarf.

The atmospheric parameters for this object inferred from Gaia eDR3 photometry assuming a pure hydrogen atmosphere are $T_{\rm eff} = 20{,}300 \pm 5400$ K and $M = 0.74 \pm 0.26\,M_\odot$. We obtained revised atmospheric parameters from the LRIS spectrum: $T_{\rm eff} = 20{,}790 \pm 250$ K and $M = 0.79 \pm 0.03\,M_\odot$, consistent with those inferred from Gaia eDR3 photometry.

The interpretation of the metal absorption lines is not straightforward for this object. Though present, we found we were unable to fit them: given the higher temperature of this H-dominated atmosphere, the metal lines in our models are extremely narrow. For example, setting $\log({\rm Ca/H}) = -6$, the Ca II K line has a full-width half maximum of approximately 0.12 Å. However, this same line in the LRIS spectrum has an equivalent width of 0.79 ± 0.11 Å, and so even with a fully saturated K line in the model, we are unable to reach such large equivalent widths. We thus speculate that the absorption is circumstellar, (and not interstellar, as it is too deep and broad to be so), similar to those in WD 1145+017 (Xu et al. 2016; Redfield et al. 2017; Le Bourdais et al. 2024). We note that there are several other unaccounted-for absorption features in the spectrum of this object, which can also be additional circumstellar absorption features. But, suspecting them to be artifacts from sky subtraction like in WD J0923+7326, we currently reserve our comments on these features.

Follow-up high-speed photometric observations were performed with CHIMERA and the McDonald ProEM. Some results are shown in the third panel from the top in Figure 6). A variety of activity is evident. The first CHIMERA data shows a consistent low-amplitude variability with a shallow but prominent dip. The ProEM light curve obtained a month later displays a deeper dip lasting around $\approx$20 minutes. The "slanted" morphology of this transit is particularly intriguing. The final CHIMERA data, however, lacks any variability. More recent high-speed photometric observations show enhanced variability (suggestive of significant debris activity), followed by a period of dormancy. These results will be presented in forthcoming work (see Guidry et al. 2024).

4.1.5. WD J1237+5937

This object appears as a candidate white dwarf only in the Gaia eDR3 catalog (Gentile Fusillo et al. 2021b). A long-timescale dip is evident in the ZTF light curve. Such a prominent photometric variability results in it being among the top 1% sources. In the η–S_P diagram, this object sits firmly in the third quadrant among the other transiting debris systems, with the long-timescale transit being well-resolved in ZTF cadence. In the LRIS spectrum (fourth panel from the top in

Figure 5), Balmer and Ca II K (along with several other metal) absorption lines are prominent, making this object a DAZ.

The atmospheric parameters for this object inferred from Gaia eDR3 photometry assuming a pure hydrogen atmosphere are $T_{\rm eff} = 6490 \pm 870$ K and $M = 0.59 \pm 0.28\,M_\odot$. The revised atmospheric parameters obtained from modeling the LRIS spectrum are $T_{\rm eff} = 6480 \pm 75$ K and $M = 0.47 \pm 0.06\,M_\odot$, consistent with those inferred from Gaia photometry.

Similar to WD J1302+1650, we fit the long-timescale dip in ZTF with the AHS function, to the combined ZTF-g and r data in terms of relative flux. The result is presented in the bottom panel of Figure 7. The inferred depth is $\approx 30\%$. The ingress and egress times are 25 days and 117 days, respectively. Here, too, the ingress is significantly shorter than egress, making collision between debris a possible cause behind the dip. However, unlike WD J1302+1650, the light curve for this object appears "smoother" with no obvious indication of shorter timescale activity (though the photometric error bars are also larger). No significant variability is seen in the high-speed photometric follow-up (Figure 6).

The reason behind such a behavior is unclear. The long-timescale dip might still be a result of a brief span of very high debris activity generated through collisions, followed by a period of quiescence (as seen in other transiting systems, like in Aungwerojwit et al. 2024). A different, though related, cause can be collisions between asteroid fragments on wide and eccentric orbits during the earlier phases of debris disk formation, a process called collisional grind-down (see for example Brouwers et al. 2022). This can produce dust and debris, potentially inducing a long-timescale dip simply from its long-period orbit. In such a case, we would expect the transit to recur at the orbital period. However, the period can be too long for the current baseline. For example, a modest semimajor axis of 4 au leads to an orbital period of about 10 yr.

We identify several metal absorption features in the spectrum, with corresponding abundances: $[{\rm Ca/H}] = -7.95 \pm 0.09$, $[{\rm Mg/H}] = -6.24 \pm 0.09$, $[{\rm Al/H}] = -7.79 \pm 0.24$, and $[{\rm Fe/H}] = -6.76 \pm 0.11$. The Ca and Mg abundances are consistent with the distribution reported in Xu et al. (2019a) for DAs. The estimated net mass accretion rate is $\log(\dot{M}) \simeq 9.08$. This is broadly consistent with the accretion rate distribution for H-dominated white dwarfs reported in Xu et al. (2019a), more so with the dusty scenario (Table 6 in their paper).

4.1.6. WD J1013–0427

Similar to the previous object, this source appears as a candidate white dwarf only in the Gaia eDR3 catalog (Gentile Fusillo et al. 2021b). The ZTF light curve bears a qualitative resemblance to WD J1237+5937, and shows only one long-lasting dip. Unfortunately, the ZTF light curve does not span the entire duration of the dip. We thus queried the light curve

from the Asteroid Terrestrial-impact Last Alert System (ATLAS) survey. We also present the light curve from the last three seasons of the Catalina Real-time Transient Survey[27] (CRTS; Drake et al. 2009) which shows the behavior of the object pre-transit. These are presented separately in Figure 8. The dip is seen to last for about two years, which is by far the longest known transit duration in such systems. We note here that, though not shown, CRTS coverage goes back to the year 2005 and another transit event is not seen. This sets the lower limit of recurrence of the transit to around 20 yr.

The object appears in the top 1% due to this significant photometric variability. This object also has the lowest and most negative values of η and S_P respectively (thus, the most extreme object in the third quadrant). The LRIS spectrum, with prominent He, H, and metal (like Ca II K) absorption lines, shows it to be a DBAZ. We performed high-speed photometric follow-up with both CHIMERA and PRISM (Figure 6) to look for any short-timescale variability. However, no variability is seen in these observations to a limit of $\sim 1\%$ amplitude.

The atmospheric parameters estimated from the Gaia eDR3 photometry assuming a pure He atmosphere is $T_{\rm eff} = 16{,}300 \pm 2500$ K and $M = 0.47 \pm 0.13\,M_\odot$. We model the LRIS spectrum to obtain the revised atmospheric parameters of $T_{\rm eff} = 21{,}900 \pm 260$ K and $M = 0.64 \pm 0.03\,M_\odot$. Though the inferred mass is broadly consistent with that from Gaia photometry, the revised temperature is significantly hotter.

Absorption features from Ca, Si, and Mg were detected in the spectrum. The abundances of these three metals inferred from the spectral modeling are: $[{\rm Ca/He}] = -5.37 \pm 0.04$, $[{\rm Si/He}] = -4.10 \pm 0.01$, $[{\rm Mg/He}] = -4.05 \pm 0.04$. These abundances are broadly consistent with the ranges reported in Xu et al. (2019a), more so with the dusty scenario. From the abundances, we obtain $[{\rm Mg/Ca}] = 1.32$ and $[{\rm Si/Ca}] = 1.27$. We compare this to the distribution of white dwarfs in the $[{\rm Mg/Ca}]$—$[{\rm Si/Ca}]$ space, as shown in Figure 4 in Xu et al. (2019a). The object appears well consistent with the distribution. The estimated net mass accretion rate is $\log(\dot{M}) \simeq 9.72$, also consistent with the range for DBs presented in Xu et al. (2019a).

We now draw attention to the uniqueness of this object among the others in our sample. The most unique aspect is the color-dependence of the transit: the transit depth in the ZTF-r band is shallower than that in the g band, in a statistically significant way. In Figure 8, we mark the median depths of the two bands, making the color dependence evident. This is the first candidate transiting debris system where a reddening during the transit is observed. We note that obvious color dependence is not observed in the ATLAS data. However, no conclusion can be drawn due to the large photometric errors. In addition to this, the follow-up spectra show prominent double-peaked metal emission lines (namely those of Mg I, O I, and

---

[27] http://nunuku.caltech.edu/cgi-bin/getcssconedb_release_img.cgi
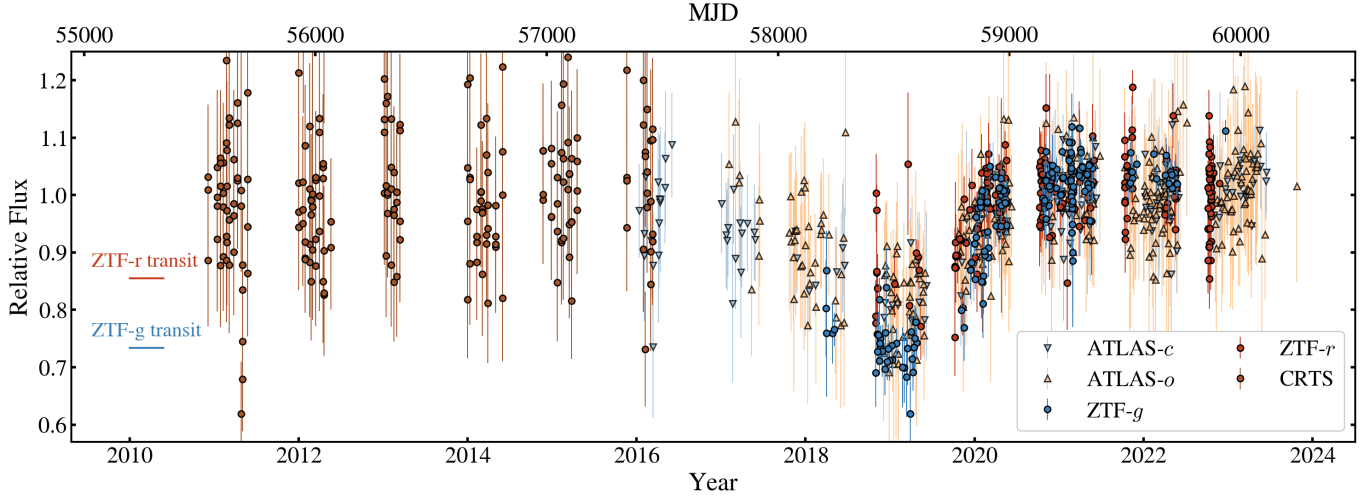
Figure 8. ZTF, ATLAS, and CRTS (last six seasons for ease of presentation) light curves for WD J1013–0427. For the purpose of this figure, the ATLAS data has been binned for better visualization of the dip. The two transit marks show the median ZTF-*r* and *g* band magnitudes for the transit duration (around MJD=58500). CRTS coverage goes back to the year 2005 and no transit behavior is seen in the full light curve.

Ca II triplet, see Figure 13 and Section 5.2), indicating a gaseous disk. Such an occurrence is rare (occurrence rate of $\approx 0.07\%$, Manser et al. 2020) with only about a couple dozen systems being known, and only a fraction of them have been studied in detail. Thus, this system is also the first (to our knowledge) to have both a gaseous disk and a transiting debris disk. These motivated further analysis of this object, which we present in Section 5.

4.2. A Long-duration Outbursting AM CVn

Here, we briefly present the remaining very interesting object in our sample. Similar to the other objects, WD J2241 +3712 (Gaia DR3 1904695262791485312) also appears in the lists of candidate white dwarfs based on Gaia DR2 and eDR3 (Gentile Fusillo et al. 2019; Gentile Fusillo et al. 2021b). This object finds its place in the catalog of Gaia catalog of photometric science alerts (Hodgkin et al. 2021), as a candidate cataclysmic variable. We note here that the ZTF light curve from IRSA, which has been used in this work for sample selection, is incomplete. We thus queried the light curve from Zubercal.[28] With the improved photometric calibration of Zubercal, a more complete light curve was recovered, which we show in Figure 3. The light curve shows a long outburst in both *g* and *r* bands (Figure 3). The variability amplitude is $\simeq 30\%$ and $\simeq 50\%$ in terms of flux in *g*, and *r* respectively. The slow and long-timescale variability is well resolved in ZTF cadence, which explains the low η metric value (see Figure 2). The large negative S_P value, however, is unexpected given the shape of the light curve. The reason behind this is the incomplete sampling in the IRSA light curve

(used to calculate the η and S_P metrics), which has an over-representation of the outbursting phase, resulting in an apparent negative S_P value. Owing to the observed variability and the position in the η–S_P metric space (thanks to the incompleteness of IRSA data), this object was targeted for follow-up spectroscopy.

The LRIS spectrum (Figure 5) shows prominent He emission lines. Such features are characteristic of AM CVns: semi-detached binary system where a white dwarf accretes from its He-dominated companion. Though AM CVns are not very rare systems, the long duration of the outburst makes this object special. Only three other AM CVns showing long-duration outbursts are known to date (SDSSJ1411+4812, SDSSJ1137+4054, and SDSSJ0807+4852 Rivera Sandoval & Maccarone 2019; Rivera Sandoval et al. 2020, 2021). The orbital periods of the known systems are in the range of ≈ 40–60 minutes. In the evolutionary track of AM CVns, this class of objects belongs to the regime where the orbit expands post the epoch of the minimum period. This results in longer orbital periods, lower mass accretion rates, and longer outburst durations compared to standard AM CVns. WD J2241+3712 is thus a candidate for this rare class of AM CVns. Being in the catalog for Gaia alerts may indicate an additional outburst during the Gaia observations.

The ZTF coverage extends to epochs both before and after the outburst, which enables estimation of the outburst duration. Visually, from the light curve (assuming the start and end of the outburst to be at MJD ≈ 58500 and MJD ≈ 59300), the approximate outburst duration is $\simeq 800$ days. This is significantly longer than the durations in the previously known systems (≈ 200–400 days). The outburst duration is expected to be positively correlated with the binary orbital period (see

---

for example Figure 4 in Rivera Sandoval et al. 2021). This makes WD J2241+3712 a candidate for one of the longest-period AM CVns. Further observations and analyses needed to constrain the orbital period and the accretion rate are beyond the scope of this paper.

5. Analysis of WD J1013–0427

In this section, we pick up from Section 4.1.6 and present our analyses of WD J1013–0427. More detailed analyses will be presented in a future paper on this object.

5.1. Modeling the Color-dependent Transit

We fit the transit of this object with the AHS function, as performed with WD J1302+1650 and WD J1237+5937. The results are shown in Figure 9. First, we combine the data from all the surveys and perform the fit to obtain the mean transit epoch, ϕ_1, and ϕ_2 (upper panel in the figure). We then fix these parameters and fit the ZTF and ATLAS light curves keeping f as the free parameter (the bottom four panels). We find that the inferred depths in the four photometric bands: 0.296 in ZTF-g, 0.218 in ATLAS-c, and 0.166 in ZTF-r and ATLAS-o are consistent with the color-dependency of the transit, with the depths decreasing with increasing bandpass central wavelength.

5.1.1. Model 1: Optically Thin and High Covering Fraction

We attempt to fit the color-dependent transit depths using a simple radiative transfer model to constrain the grain size distribution. The assumptions of this model are: (1) the dust covers the disk of the white dwarf uniformly, and (2) the dust is optically thin. These assumption stems from the long duraration of the transit (which might imply a diffused dust structure rather than a disk) and the detection of color-dependence. We denote $I_{\lambda,0}$ as the out-of-transit intensity at and per unit wavelength λ (i.e., the radiation from the white dwarf) and I_λ as the time-dependent observed intensity (the subscript λ denotes the unit of "per unit wavelength"). These quantities relate to the observed transit depth in a photometric band, D_{band} ($=1$ − Relative Flux, and same as the measurements in Figure 9), as:

$$D_{\text{band}} = \frac{\int_{\text{band}} (I_{\lambda,0} - I_\lambda)\, \lambda\, \mathcal{T}(\lambda)\, d\lambda}{\int_{\text{band}} I_{\lambda,0}\, \lambda\, \mathcal{T}(\lambda)\, d\lambda}, \tag{9}$$

where $\mathcal{T}(\lambda)$ is the instrument transmission function as a function of wavelength.[29] The transmission functions are shown in the last panel of Figure 9. In the implementation of this model, we used the best-fit WD atmosphere model to the LRIS data (shown in Figure 5) as $I_{\lambda,0}$. We obtained the
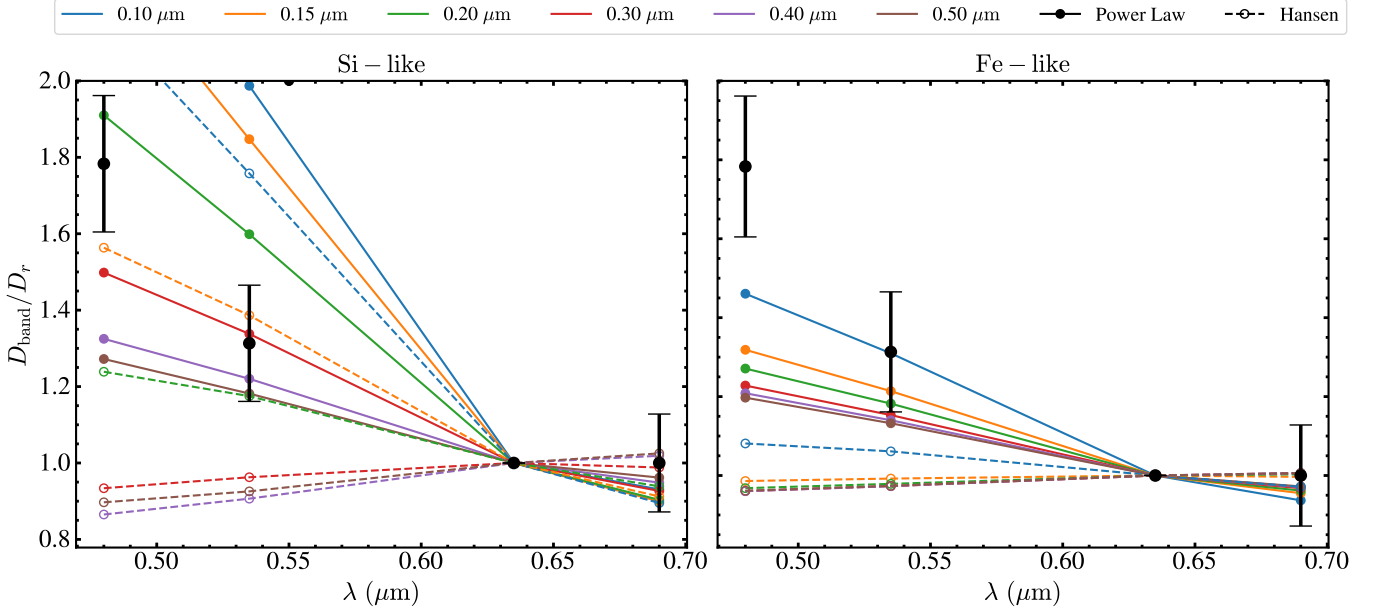

Figure 9. The light curves of WD J1013–0427 fit with Equation (8). Top panel: A combined fit of the data from all the surveys to obtain the overall transit shape. Central four panels: The fit to the data from ZTF and ATLAS individually. The parameters derived from the combined fit are fixed at the median values, with f being the only free parameter in these fits. The inferred transit depths have been mentioned in the figure. We have used the complete and un-binned ATLAS data for this fit. Bottom panel: The transmission functions, $\mathcal{T}(\lambda)$, of the survey bands and their central wavelengths.

transmission curves from the webpage of SVO filter profile services.[30]

We now consider a simple radiative transfer equation (RTE) in the optically thin limit. We denote $n(r)$ as the radius distribution of the dust grain density and $\sigma_{\text{ext}}(r, \lambda)$ as the wavelength-dependent Mie extinction cross-section. The RTE

---

[29] The factor of λ in the equation is to convert the intensity values to photon counts, which is what the detector measures. Note that an effective wavelength term (to convert the photon count to energy flux) gets eliminated while taking the ratios and, thus not included in the equations.

[30] http://svo2.cab.inta-csic.es/theory/fps/

Figure 10. The observed (black points) and analytic (Equation (12), colored lines) transit depths relative to that of ZTF-*r* for Si-like (left panel) and Fe-like (right panel) grains for the transits of WD J1013−0427 shown in Figure 9. Suspecting underestimation of the inferred depth errors, we show the 2σ error bars for the observed points here. Owing to being the reference wavelength for normalization, the point corresponding to ZTF-*r* has no error bar. This error has been appropriately propagated to the other data points. A grain radius of $\lesssim 0.3$ μm is required to explain the observed transit depths with Si-like grains. Fe-like grains are unable to explain the observed depths.

reads:

$$I_\lambda \approx I_{\lambda,0}\left(1 - L\int_{r_{\min}}^{r_{\max}} \sigma_{\text{ext}}(r, \lambda)n(r)dr\right) \quad (10)$$

where $r_{\min}$ and $r_{\max}$ are the minimum and maximum radii of the particles, and L is the net line of sight length (the assumption is that the grain properties are independent along the line of sight column). Following Hallakoun et al. (2017), we define the mean extinction cross section for the assumed grain size distribution as:

$$\overline{\sigma}(\lambda) = \frac{\int_{r_{\min}}^{r_{\max}} \sigma_{\text{ext}}(r, \lambda)n(r)dr}{\int_{r_{\min}}^{r_{\max}} n(r)dr}. \quad (11)$$

Combining Equations (9), (10), and (11), we get:

$$D_{\text{band}} = \frac{N\int_{\text{band}} I_{\lambda,0}\overline{\sigma}(\lambda)\lambda\mathcal{T}(\lambda)d\lambda}{\int_{\text{band}} I_{\lambda,0}\lambda\mathcal{T}(\lambda)d\lambda} \quad (12)$$

where $N = L\int_{r_{\min}}^{r_{\max}} n(r)dr$ is the total column density of the dust particles along the line of sight, responsible for the extinction.

Following the treatment in Croll et al. (2014), we assume two different grain size distribution functions. First is the power law function given by:

$$n(r) \propto r^{-p}. \quad (13)$$

We assume $p = 3.5$, which is expected from collisional cascade and that inferred in other setups (interstellar medium, see Mathis et al. 1977). Following the methodology in Croll et al. (2014), we fix the minimum grain size to $r_{\min} = 0.01$ μm, and calculate the transit depths for different values of $r_{\max}$. The second distribution is from Hansen (1971, Hansen distribution), which, in context of debris transits, has been used in Hallakoun et al. (2017):

$$n(r) \propto r^{\frac{1-3\nu_{\text{eff}}}{\nu_{\text{eff}}}}e^{-\frac{r}{\nu_{\text{eff}}r_{\text{eff}}}} \quad (14)$$

where ν_{eff} and r_{eff} are the effective variance and radius, respectively. Following Hallakoun et al. (2017), we use $\nu_{\text{eff}} = 0.1$ μm, $r_{\min} = 0$ and $r_{\max} = \infty$ as fixed parameters. The variable in this model is r_{eff}.

Finally, we note that the extinction cross-section, σ_{ext}, is dependent on the refractive index of the dust material. We adopt two values of refractive index of $1.7 + 0.03i$ (Si-like) and $2 + 2.5i$ (Fe-like), which may be taken as representative values for silicon and iron-dominated environments, respectively (Hallakoun et al. 2017).

The column density, N, in Equation (12) is not known apriori. Thus, we normalize the depths (both the observed and those calculated from the model) to that of a reference band (we use ZTF-*r* for our purpose) so that this factor gets eliminated. We will revisit this in a few paragraphs. Figure 10 shows the *r*-band normalized transit depths, both the observed and the model values. A satisfactory fit to all the data points
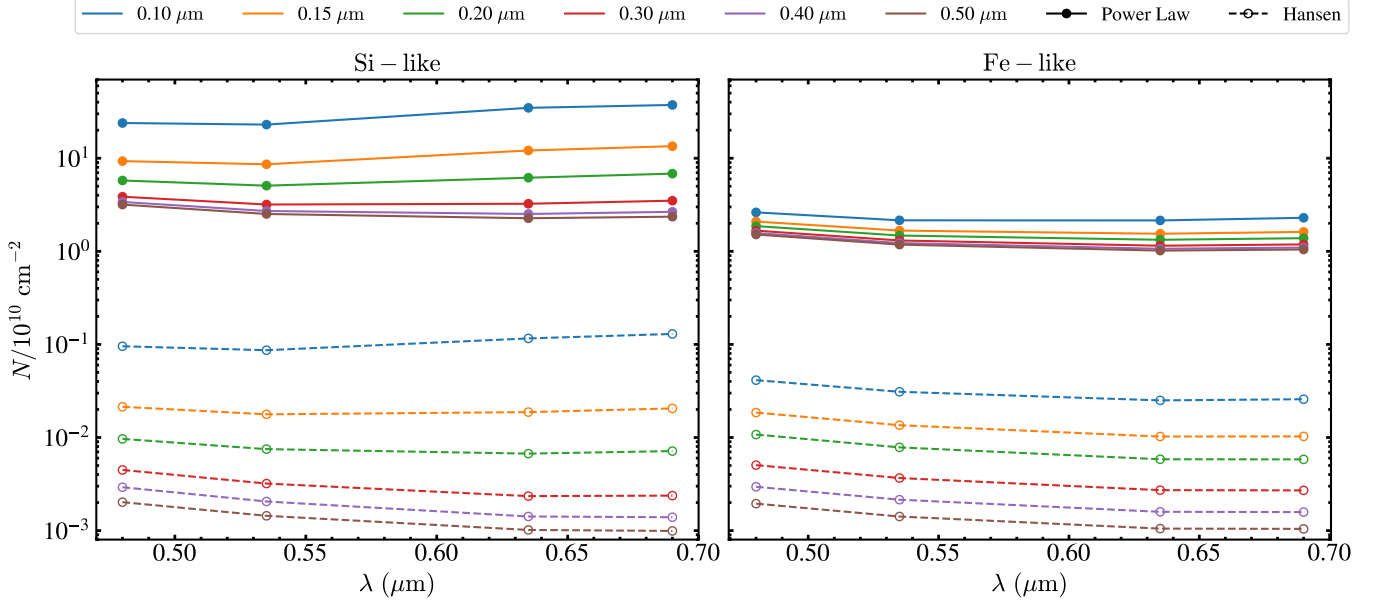
Figure 11. The dust column density estimations from the observed median transit depths over a range of grain-size parameters for Si-like (left panel) and Fe-like (right panel) grains for the transits of WD J1013–0427 shown in Figure 9. We get a very broad estimate of 10^7–10^{11} cm^{-3}, but it heavily depends on the assumed grain-size distribution.

could not be obtained with a single grain model. Therefore, we employ a heuristic comparison of the model with the data. We compare the model predictions to the observed data for a wide range of grain-size parameters (namely, r_{max} and r_{eff}), for both the refractive index cases (as shown in the figure). For ease of readability, we use the same set of parameter values for both grain distributions. We caution, however, that the parameters of the two models represent different quantities, thus a one-to-one comparison is not possible.

With Si-like grains (left panel in the figure), the r-band normalized depths from the model span the correct range of values as the observed data. However, the models fail to fit the depths of ZTF-g and ATLAS-o simultaneously. Qualitatively the best match to the data points appears to occur with $r_{max} \approx 0.2 - 0.3\,\mu$m with power law distribution, and $r_{eff} \lesssim 0.15\,\mu$m in Hansen-distribution. We call these the "best-match" parameters. These are significantly smaller than the constraints in other systems. This is, thus, the first system that indicates the abundance of small-sized grains in the circumstellar material. This may also indicate that the dust responsible for the obscuration are situated at a sufficiently wide orbit (at least a few solar radii, comparing with the results from Xu et al. 2018), otherwise, such small-sized grains would be heated to sublimation by the white dwarf.

The match to the observed data worsens with Fe-like grains (right panel in the same figure). A reasonable match to the g-band depth would require the grain size parameter to be $<0.05\,\mu$m; an abundance of such small-sized grains is highly unlikely owing to their significantly lesser chance of survival.

This makes the environment unlikely to be Fe-dominated. A worsening of fit with Fe-like refractive index was also seen in Hallakoun et al. (2017), which may indicate against a Fe-dominated environment in debris scenarios.

With assumed grain size parameters, we can use Equation (12) to estimate the column density of the dust particles responsible for the extinction, given the observed D_{band} values. Figure 11 shows the inferred column densities over the same range of parameters as used in Figure 10. With the power law distribution, the column densities lie in the range of $\sim10^{10}$–10^{11} cm^{-2} with both Si-like and Fe-like grains. With the Hansen distribution, the calculated column density, however, is significantly smaller and lies in the range of $\sim10^7$–2×10^9 cm^{-2}. This is a consequence of the Hansen function being biased towards larger grain sizes, as the same transit depth can be achieved with a smaller quantity of larger grains (with larger extinction cross sections). Considering the "best-match" parameters, the corresponding estimation of the column density is in the range of $\sim10^8$–10^{11} cm^{-2}. This exercise shows that the column density estimations are heavily dependent on the assumed grain size distribution. Thus, future observations providing independent constraints on the circumstellar column density can provide valuable information on the underlying grain size distributions.

5.1.2. Model 2: Optically Thick and Low Covering Fraction

Studies of other systems with transiting debris disks in the past have favored a model different than the assumptions in Model 1. Past systems are seen to mostly indicate optically thick disk covering only a small fraction of the white dwarf

disk. However, none of the previous systems had a detected reddening. But we still use such a model to check if it can explain the observed color dependence.

Here we consider the model developed in Appendix A of Izquierdo et al. (2018). Briefly, the model assumes a disk with a vertical profile which is optically thick at the center, but becomes thinner at the edges. The model assumes that the disk core is completely opaque (high τ), and completely transparent beyond the height, h, where $\tau = 1$. This height h_λ is different for different wavelengths, owing to a wavelength dependence of the scattering cross section, which leads to a power-law parametrization of optical depth with index α (their Equation (A4)). The transit depth is then modeled as the fraction of area of the white dwarf covered by the projection of the disk core, which is a rectangle. We note here that the model is deceptively simple as it seemingly avoids any grain size distribution details. But all the grain size information are wrapped in the α parameter.

This formalism gives, for a given wavelength (in this context the central wavelength of a band), the transit depth approximately as:

$$D_\lambda = \frac{4}{\pi} \frac{h_\lambda}{R_{\rm WD}} \sqrt{1 - \left(\frac{h_\lambda}{R_{\rm WD}} \right)^2}, \qquad (15)$$

where $R_{\rm WD}$ is the white dwarf radius. Note that there is an error in the original paper where they missed a factor of 2. Fortunately, the correction works in favor of the model. With the inferred depths, solving for h_λ gives $h_g/R_{\rm WD} = 0.239$, $h_c/R_{\rm WD} = 0.174$, and $h_r/R_{\rm WD} = h_o/R_{\rm WD} = 0.132$.

The consequence of these values is that they break down the assumption of $|h_\lambda - h_r| << h_r$ (mentioned right after Equation A5 in their paper). Thus, the remaining equations in the paper are not strictly valid and require modifications. However, we note that as $h_\lambda/R_{\rm WD}$ is much less than unity, the square root term in Equation (15) is very close to unity and can just be dropped for simplicity. Then, following the same convention (taking the r band as the reference), we have (combining with their Equation (A3)):

$$D_\lambda - D_r = \frac{4\alpha}{\pi} \frac{1}{\ln(\tau_{r,0})} \ln \left(\frac{\lambda_r}{\lambda} \right) \left(\frac{h_r}{R_{\rm WD}} \right) \frac{1}{1 + h_\lambda/h_r} \qquad (16)$$

where $\tau_{r,0}$ is the mid-plane optical depth in the r band. This can then be used to estimate $\tau_{r,0}$. Using ZTF-g band depth, for example, we get $\tau_{r,0} \approx e^{0.15\alpha}$ which lies in the range of 1.16–1.82, depending on the value of α chosen. Note that these values are quite low (compared to estimates of $\gtrsim 200$ for WD 1145+017 in Izquierdo et al. 2018) and also does not quite satisfy the main assumption of the model of $\tau_{0,r} >> 1$. This already hints that this model may not be appropriate for this object, and also hints at a significant optically thin component of the transiting material.

For better visualization, we use $\tau_{0,r}$ in Equation (16) as a parameter to compute $D_\lambda - D_r$ and compare with the observed
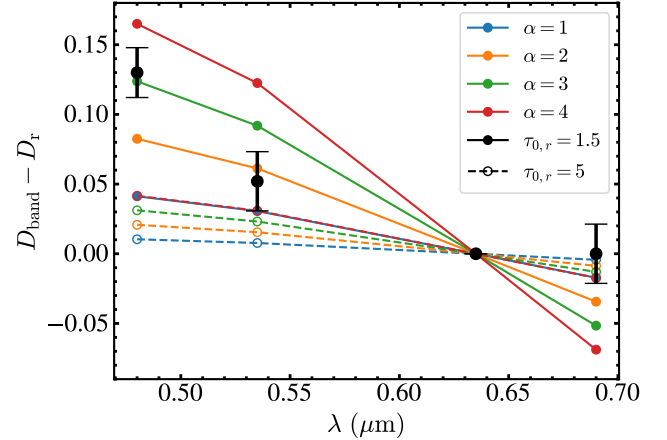

Figure 12. The observed (black points) and analytic (Equation (12), colored lines) transit depths excess to that of ZTF-r for two representative values of $\tau_{r,0}$ and four integer values of α. As with Figure 10, we show the 2σ errors, with the error in the ZTF-r band measurement appropriately propagated to the other data points.

values. We show this in Figure 12. It is clear that for any high value of $\tau_{r,0}$, the model under predicts the depth in the blue bands. The model agrees broadly with the blue-side data for low values of $\tau_{r,0}$, but significantly underestimates the ATLAS-o depth. Also, as mentioned earlier, the assumptions of the model starts to break down here. Even with $\tau_{r,0} = 1.5$, we see that one needs $\alpha \gtrsim 3$ to explain the observed depths. Such a high α value is only possible when there is a large abundance of small grains with size definitely less than $x \lesssim \frac{\lambda}{\pi} \approx 0.2\ \mu$m. This is in agreement with that inferred from the optically thin model.

Note that, in reality, WD J1013-0423 maybe somewhere in between the two models discussed above. Additionally, the viewing angle may not be totally edge on. Such analyses are beyond the scope of this paper.

5.2. Modeling the Emission Lines

Several double-peaked emission lines are evident in the LRIS spectrum of WD J1013–0427 indicating a gas disk: The most prominent emission lines are the Ca II triplet at 8498, 8542, 8662 Å, the O I triplet at 7776 Å, and Mg I triplet at 5175 Å. We show the emission lines from the spectra obtained at all five epochs in Figure 13. No significant variation of the emission line profiles across the different spectra was observed. The emission profile encodes essential features of the disk structure. Fitting the profile with an appropriate disk model can enable constraining essential disk properties like eccentricity and semimajor axes, among others. We undertake this exercise in this section. Among the prominent emission features, only the Ca II 8662 Å feature is not blended with other nearby lines. In this work, we use only this line for analysis and reserve detailed modeling of all the emission lines
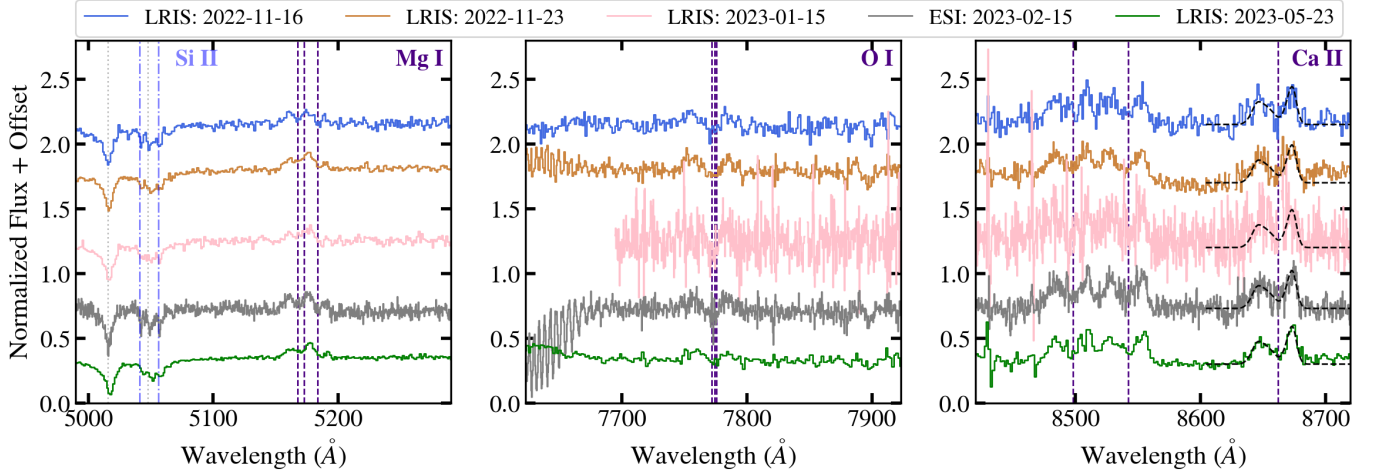
Figure 13. The emission lines detected in the spectra of WD J1013–0427: magnesium (Mg I, left), oxygen (O I, center), and calcium (Ca II, right). In the panel for Mg I, we also show the detected Si II absorption around a He line to caution the readers not to confuse the net "triple-peaked" absorption feature as a signature of Zeeman splitting. For the Ca II 8662 Å emission line, we over-plot the disk model (derived and discussed in Section 5.2) with the median MCMC fit parameters (Table 6).

for the future. We use the spectrum with the best signal-to-noise, which is the LRIS spectrum obtained on 2023 May 23.

We first note a few observed properties that are important in formulating the disk model. First, the intensities of the three lines of Ca II triplet appear to be of similar intensities in the spectra, though their transition probabilities are vastly different. Second, the Ca II 8662 Å profile shows a deep dip at the line center. These properties are similar to a few other systems (e.g., Gänsicke et al. 2006) and suggest that the disk is optically thick. Furthermore, we note the asymmetry in the two peaks of the emission line, which hints at an elliptical orbit of the gas disk. In the next few paragraphs, we formulate a generalized disk model which incorporates both these effects.

We base our disk model primarily on the works of Horne & Marsh (1986), Gänsicke et al. (2006), and Goksu et al. (2024). We assume the disk to be a Keplerian ellipse and finite in extent, with inner and outer semimajor axes of a_{in} and a_{out}, respectively, and eccentricity e. We model the disk as consisting of N confocal Keplerian rings. We chose $N = \text{floor}[(a_{out} - a_{in})/R_{WD}]$, where R_{WD} is the radius of the white dwarf, which proved enough to sample the disk adequately. We subdivide each ring into a thousand azimuthal angular sections (of equal angular extent) measured from the focus where the white dwarf resides. For each of the sections, the emission profile takes the form:

$$\Delta L(\boldsymbol{r}) = S_\nu(1 - e^{-\tau_\nu})\Delta A = \frac{j_\nu}{\alpha_\nu}(1 - e^{-\alpha_\nu \Delta z/\cos(i)})\Delta A \quad (17)$$

where ΔL is the luminosity, S_ν is the source function with j_ν and α_ν being the emissivity and absorptivity respectively, τ_ν is the optical depth with Δz being the vertical path through the disk and i is the inclination. ΔA is the differential area of the ring element. Note that each of these quantities is a function of the

position vector of the ring element, $\boldsymbol{r}$. This is implied and we drop this explicit dependence from the subsequent formulae.

We employ photoionization equilibrium to calculate the emissivity, as done in Goksu et al. 2024. This makes $j_\nu \sim \sigma_i c n_\gamma n_g \phi_\nu$, where ϕ_ν is the line profile, and n_γ and n_g are the ionizing photon and gas densities, respectively, σ_i is the ionization cross section and c is speed of light. However, for an optically thick system, this may not be the case and bound-bound photoexcitations may also contribute. This makes n_γ as some effective photon density. Also, $\alpha_\nu \sim \sigma_a n_g \phi_\nu$, where σ_a is the absorption cross section. This makes $S_\nu \propto n_\gamma$. Assuming the disk to be sufficiently thin, we neglect the variation of Δz with position. Continuity equation applied along the ring makes

$$n_g = n(a)\frac{(\sum \Delta l)/v}{\sum(\Delta l/v)} \quad (18)$$

where v is the Keplerian velocity, Δl is the length of the ring element, $n(a)$ is the average density of the ring with semimajor axis a, and the sum is over all the ring elements. Also, $\Delta A \approx \Delta l \Delta a \propto \Delta l$ as the rings are nearly uniformly spaced (thus Δa, the radial extent of a ring is roughly a constant). We also assume $n_\gamma \propto r^{-\alpha}$. This makes our final differential luminosity formula:

$$\Delta L = C_1 r^{-\alpha}(1 - e^{-C_2' n(a)\frac{(\sum \Delta l)/v}{\sum(\Delta l/v)}\phi_\nu})\Delta l \quad (19)$$

where C_1 and C_2 are normalization factors. Using Equations (18) and (19) in Horne & Marsh (1986), we can further write:

$$C_2' n(a) \approx \left[\frac{\pi e^2}{m_e c}f\frac{c}{\nu_0}N_{Ca}(a)\right]\frac{1}{\cos(i)} \quad (20)$$

where f is the oscillator strength, m_e and e are the mass and charge of electron, N_{Ca} is the vertical column density of calcium, ν_0 is the rest emission frequency, and i is the inclination angle which is a parameter in our model. The variation of N_{Ca} with a can be complicated. Standard disk models like Shakura-Sunyaev predict a monotonic power law decrement with distance. However, results of Goksu et al. (2024) hint at a possibility of deviation from such behavior and a more complex variation of N_{Ca} with distance. In this work, for simplicity, we assume N_{Ca} to be a constant. We recognize that this may not be an ideal assumption. This, along with other possible unaccounted parameters (like varying eccentricity) can indeed alter several inferences. However, the current data with no prior knowledge of any of the parameters, is unsuitable for constraining the additional parameters. Thus, we limit ourselves to a smaller number of parameters and keep a more detailed model for future work. With this simplification, we call the term in the parentheses as C_2, and use it as a parameter in our model. We note here that in the limit of small optical depth, Equation (19) reduces to an expression similar to Equation (3) in Goksu et al. (2024). We sum the differential luminosity for all the rings' elements to obtain the final spectrum.

For ϕ_v, we use the prescription by Horne & Marsh (1986) for optically thick emission lines. We assume a Gaussian profile of the local emission. The line-of-sight Doppler velocity of a ring element is given by the local Keplerian velocity in an elliptical orbit:

$$v_D = \sqrt{GM_{WD}\left(\frac{2}{r} - \frac{1}{a}\right)} \sin(\theta)\sin(i) = v_K(r)\sin(\theta)\sin(i) \tag{21}$$

where θ is the angle between the velocity vector and the orbital plane-projected line of sight, and M_{WD} is the mass of the white dwarf. The standard deviation of the Gaussian velocity profile, Δv, is given by both the thermal motion and the shear component of the disk:

$$\Delta v = v_{th}[1 + Q \sin^2(i)\tan^2(i)\sin^2(2\theta)] \tag{22}$$

where Q is the ratio of shear to thermal broadening, which we assume to be unity (Horne & Marsh 1986), and v_{th} is the thermal velocity dispersion. Previous studies have shown that the gas temperatures in the vicinity of the white dwarf are significantly higher than either the blackbody or the dust temperatures at that distance (see, for example, Figure 9 in Xu et al. 2024). We use the analytic prescription laid out in Melis et al. (2010, solving Equations (2), (7), and (8) in their paper), to calculate the gas temperature, T_g. Their results have been shown to agree with numerical calculations (Cloudy, Xu et al. 2024). The thermal velocity broadening is then calculated as $v_{th} = \sqrt{k_B T_g/m_{Ca}}$, where m_{Ca} is the mass of the Calcium atom.

The model has been implemented in the Cartesian coordinate system, with the origin on the WD. The $+x$ has been defined along the line joining the WD and the periastron, and the velocity at the periastron has been taken to be along $+y$. All angles are measured counterclockwise from the x-axis. The velocity vector is then given by:

$$\boldsymbol{v} = \frac{v_K(r)}{\sqrt{1 + e^2 + 2e\cos(\beta)}}[-\sin(\beta)\hat{x} + \{e + \cos(\beta)\}\hat{y}] \tag{23}$$

where β is the focal azimuthal angle, the line of sight is then parameterized by the angle ϕ in the same convention for angles. Appropriate vector products have been used to determine relative angles between different vectors. We also adequately down-resolved the model emission profile to match the LRIS resolution before performing any fit.

We attempt to find best-fit values of this parameter using Python implementation of Markov Chain Monte Carlo (MCMC) emcee (Foreman-Mackey et al. 2013). We consider a region of ± 2000 km s^{-1} around the Ca II 8662 Å rest wavelength for this purpose. We subtract the WD spectral model from the data in this wavelength range to generate the data for the MCMC. We work in the units of $(10^{-17}$ erg s^{-1} cm^{-2} Å$^{-1})$ for reasonable pre-factors. The primary variables of our model are: e, a_{in}, a_{out}, ϕ, $\log(C_1)$, $\log(C_2)$, α, and i. We include another parameter, v_c, to account for the overall Doppler shift of the line centroid. We use a simple log-likelihood function of

$$\mathcal{L} = -\frac{1}{2}\sum_n \left(\frac{f_n - y_n}{\sigma_n}\right)^2 \tag{24}$$

where y_n and σ are the data and errors, and f_n is the model output. We employ a broad range of uniform priors on all the parameters. We have used 30 walkers and 8000 steps for the MCMC. We estimate "guess values" for the parameters based on trial-and-error and smaller MCMC runs. We initialized the walkers by randomizing the parameters uniformly over $\pm 30\%$ around the guess values. The summary of the MCMC run, along with the results, are provided in Table 6. We show the model fit to the data in Figure 14 and the corner plot in Figure 15.

Before any further discussion, we note the existence of degeneracies between several parameters in our model. Some of the parameters may also be dependent on the finer features of the emission profile, which are not captured by the current data due to inadequate signal-to-noise (the high-velocity wings, for example, determine the inner orbit of the disk). Thus, the results (especially the errors) in Table 6 should be interpreted with caution. However, we can extract a few essential information about the system from the parameters with seemingly good constraints. The disk seems to be compact with an inner and outer semimajor axis of

Table 6
Summary of the MCMC Run Performed to Fit the Ca II 8662 Å Emission Line Profile of WD J1013–0427 with the Disk Model Derived in Section 5.2

Parameter	Priors	Initial ($\pm 30\%$)	Result
e	[0, 1]	0.2	$0.27^{+0.08}_{-0.07}$
$a_{\rm in}/R_{\rm WD}$	[1, 150]	15	$19.03^{+8.82}_{-11.01}$
$a_{\rm out}/R_{\rm WD}$	$[a_{\rm in}, 300]$	60	$48.46^{+6.82}_{-5.44}$
ϕ (rad)	$[0, 2\pi]$	4.5	$4.68^{+0.54}_{-0.51}$
$\log(C_1)$	$[-5, -1]$	-3	$-2.65^{+0.33}_{-0.29}$
α	$[-3, 3]$	0	$-0.37^{+0.32}_{-0.41}$
i (rad)	$[0.0, \pi/2]$	1	$1.38^{+0.08}_{-0.10}$
$\log(C_2)$	[0, 15]	8	$6.88^{+5.34}_{-4.43}$
v_c(km s^{-1})	[0, 100]	40	$43.88^{+31.81}_{-29.44}$

Note. The ϕ_v in Equation (19) has been defined in units of km s^{-1}. Thus relating C_2 from this table to the other parameters of Equation (20) requires proper consideration of this factor. Using $f \simeq 0.1$, we get $N_{\rm Ca} \approx 10^{12} C_2$ cm^{-2}.

$\simeq 20\,R_{\rm WD} \approx 0.2\,R_\odot$ and $\simeq 50\,R_{\rm WD} \approx 0.5\,R_\odot$ respectively. It has also a non-negligible eccentricity of $\simeq 0.25$. These values are broadly consistent with similar estimates in other systems (Gänsicke et al. 2006; Melis et al. 2010), though the outer semimajor axis appears relatively more compact. We also find that the inclination of the system is $\gtrsim 80°$. Such a high inclination is consistent with this object being a transiting debris candidate. We also emphasize that, as seen in Figure 14, the model has been able to capture the emission profile very well. This demonstrates the promise for future application of this model to similar data of other objects.

An apparently puzzling result is the inferred value of the photon index α being $\simeq 0$. Physically, α determines the variation of the ionizing flux with distance, and in free space, the expected value is $\alpha = 2$. A value consistent with zero, on the contrary, implies that the photon flux remains nearly constant with distance, which is physically not possible. This may imply that one or more assumptions in this exercise is not valid for this system. For example, recombination may not be the only source of radiation. In high-density environments, collisional excitation followed by radiative decay may contribute to the flux. Additionally, we have purposefully neglected effects like the variation of density with distance, which may affect the value of α (and also possibly other parameters, see for example the differences between Gänsicke et al. 2006 and Goksu et al. 2024 about WD J1228+1040).

5.3. Discussion

Despite the above efforts, several aspects of the WD J1013–0427 system remain unclear. The first among them is the shape of the transit. Referring to the AHS fit to the transit profile (top panel in Figure 9), we see that, unlike the other objects, the inferred ingress time to the transit ($\simeq 419$ days) is
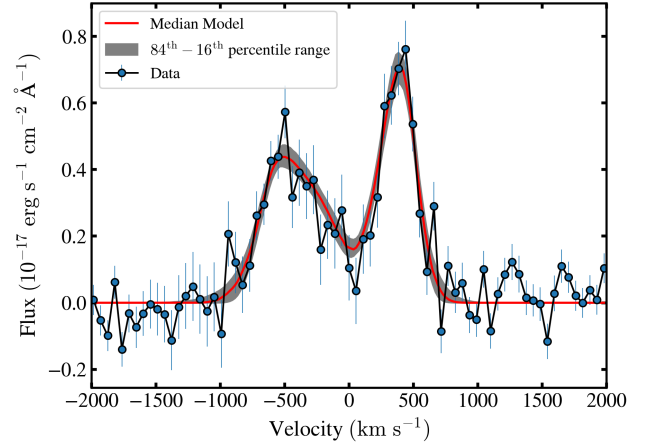

Figure 14. The MCMC fit of the disk model to the model-subtracted Ca II 8662 Å emission line profile (from the LRIS observation on 2023 May 23rd) for WD J1013–0427.

about a factor of three longer than the egress time ($\simeq 144$ days). This is in contrast to what is naturally expected in events like collisions between debris in the disk, where the production of obscuring dust is faster than their re-condensation (leading to shorter ingress time). This makes us consider the possibility of collision events involving larger objects (like planets) on wider orbits than typical transiting debris systems. The timescale of such an event may be larger (owing to both the larger dimensions of the objects at play and the event possibly taking place at a much wider orbit) and consistent with the net transit duration in WD J1013–0427 (see for example such a recently discovered event in a G2 dwarf system, Kenworthy et al. 2023). The specifics of the impact geometry and parameters may result in a wide range of ingress and egress durations. Such events, however, are expected to be associated with significant infrared excess either during or before the transit. WD J1013–0427 is ultimately too faint at the near-infrared for us to draw meaningfully assess the variability of its dust disk from its WISE light curve[31] (Guidry et al. 2024), which is consistent with non-detection of any source within error bars throughout (thus not shown).

Another related cause, similar to WD J1237+5937 (Section 4.1.5), can be the collision of asteroid fragments at wide and eccentric during collisional grind-down (Brouwers et al. 2022). The total available light curve baseline sets a lower limit on the period at approximately 20 yr. This yields a corresponding lower limit on the orbital semimajor axis of about 6 au. In such a case, the eccentric asteroids may interact with the detected compact gas disk, inducing drag that aids in their circularization (see for example Malamud et al. 2021).

---

[31] Forced aperture photometry was performed at the source position in publicly available time-resolved unWISE images (Meisner et al. 2018), as described in Tran et al. (2024), to genarate the light curve.
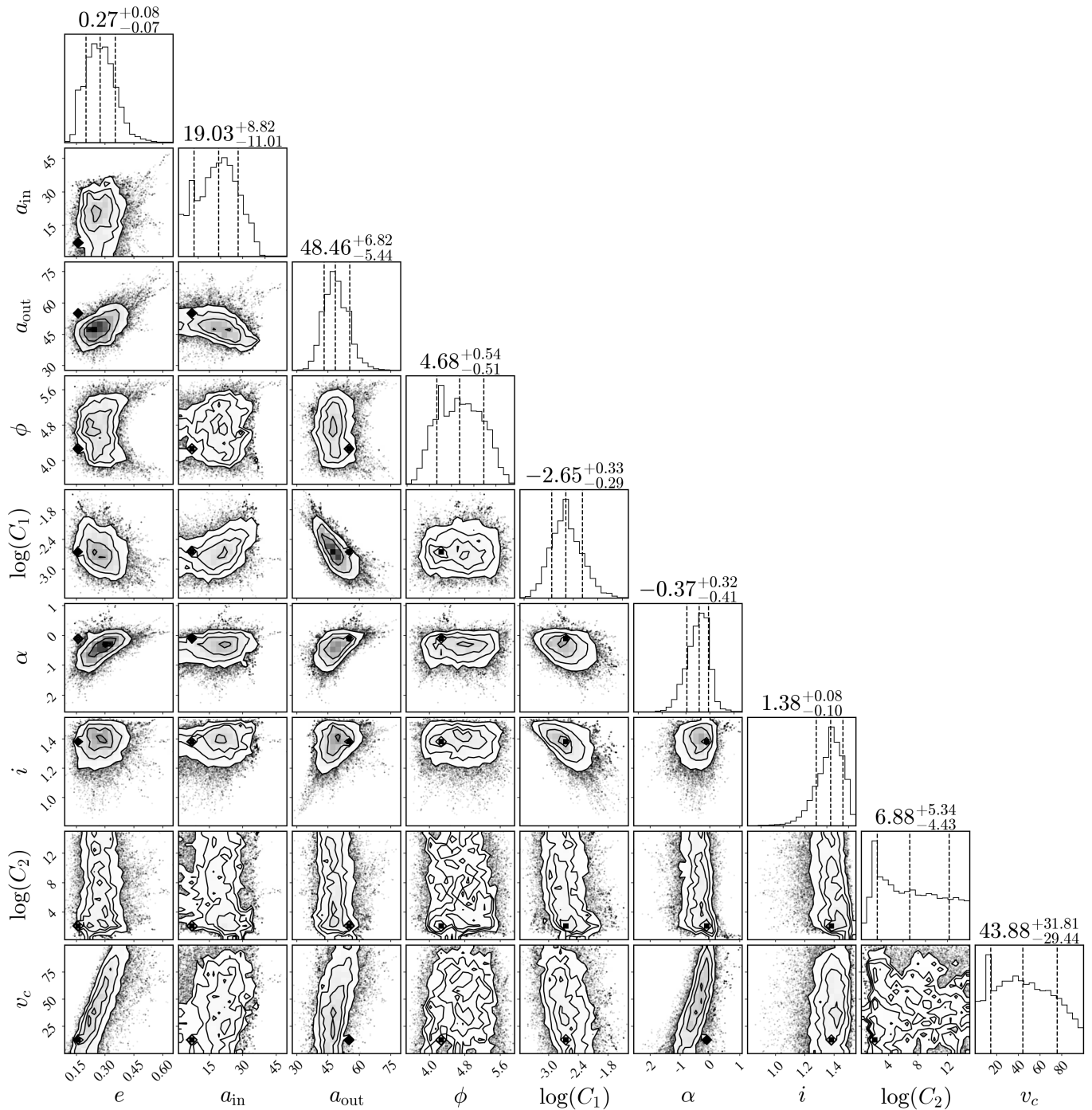
Figure 15. The corner plot for the MCMC run discussed in Section 5.2. Satisfactory constraints are obtained for the three main parameters: eccentricity, e, and the inner and outer semimajor axes, a_i and a_o.

This can, in turn, also be another source of the long-timescale dip. The sequential impact of the asteroid fragments may cause dust creation or ejection leading to a long ingress time, followed by a rapid dissipation of the material into a disk resulting in the shorter egress duration. This scenario can only

be confirmed if a second dipping event is seen in future light curves.

We conjecture a second possibility, where the observed transit results from the precession of a debris disk. This may occur when a section of the debris orbit is crowded/puffier and

it crosses the line of sight once over the precession period. The morphology of the overdense region may then govern the ingress and egress. We use Equation (1) in Manser et al. (2016) to calculate the precession period in WD J1013–0427. In an extended disk, the precession period of the inner and outer regions may be significantly different. We note here that we do not have any constraint on the extent of the dust disk. As a proxy, we use the extent of the gas disk inferred in the previous section. This yields precession periods of 0.2 yr and 20 yr for the inner and outer edges of the disk, respectively. The debris disk, responsible for the target, however, may have a larger orbit and thus longer precession period. This is also indicated by the presence of small-sized dust grains (see Section 5.1). For example, the precession period, being a strong function of the semimajor axis shoots up to 65 yr at $1\,R_\odot$, the typical tidal radius of a WD. Thus, if it is for this reason, the temporal baseline of the current data may not be sufficient to observe another transit.

6. Comparison of Accretion Rates with Other Polluted White Dwarfs

The growing population of white dwarfs with transiting debris enables statistical study of their properties. Here, we briefly compare the inferred accretion rates of the white dwarfs transiting planetary debris with those of the larger population of metal-polluted white dwarfs. We downloaded the list of DA, DB, and DZ white dwarfs having "at least one optical spectrum available" from MWDD (Dufour et al. 2017), only for those objects for which the values for temperature, $\log(g)$, and mass are available. We have also rejected upper limit abundance values. Additionally, we impose a distance cut of 500 pc and a magnitude cut of Gaia $G < 19$ to (1) be consistent with the distance limit of this work, and (2) to ensure that the underlying spectra used to derive the abundnaces are reliable (given most of the measurements are with SDSS spectra). For an unbiased comparison between the different data points, it is necessary to have a consistent calculation of accretion rates across objects. Thus, for this purpose, we used the abundance of a single metal to estimate the total accretion rate assuming an abundance ratio. We first used the measured Mg abundances and assumed a bulk Earth-abundance Mg mass fraction of 15.8% (Allègre et al. 2001). The justification to use Mg is that its abundance is relatively more stable than the other metals (see, for example, Xu et al. 2019a). However, many of the polluted white dwarfs (including a few among the transiting debris candidates) do not have measured Mg abundances. Thus, we performed a second estimate using Ca, assuming an Earth abundance ratio of 1.67% (Zuckerman et al. 2010). The same methodology for accretion rate calculate as described in the beginning of Section 4.1 has been employed to ensure consistency in the accretion rate estimates. The comparison is provided in Figure 16. We label the H and
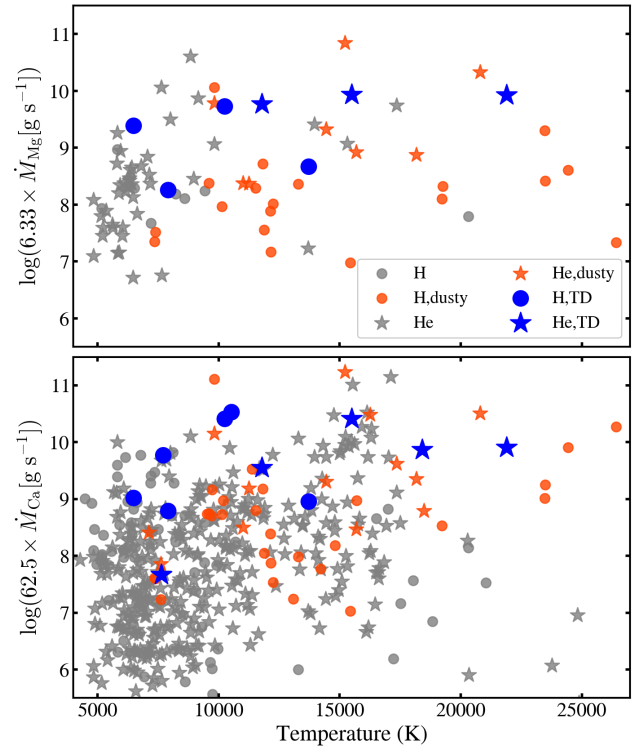
Figure 16. Inferred accretion rate as a function of temperature for the transiting debris systems in comparison with the pool of metal polluted white dwarfs from MWDD (Dufour et al. 2017). "Dusty" stands for objects with detected infrared excess. The transiting debris systems tend to have a high accretion rate.

He white dwarfs differently and also distinguishes between dusty and non-dusty systems, as done in Xu et al. (2019a). We used the parameter "infrared excess (disk)" in MWDD for this purpose. We found that the MWDD list of dusty white dwarfs is incomplete. Thus, in addition, we referred to a list of dusty systems independently compiled by S.X. (as a part of Xu et al. 2019b and subsequent updates), and combined them.

Overall, the accretion rates inferred for the transiting debris systems are on the higher side. Most of them have an estimated total accretion rate of $\gtrsim 10^9\,\mathrm{g\,s^{-1}}$. The rates for the He white dwarfs are broadly consistent with the other metal-polluted He white dwarfs for a given temperature (estimates of accretion rates for He white dwarfs are usually higher than H white dwarfs, possibly due to longer diffusion timescales in the former, see for example Farihi et al. 2012, and convective overshoot effects, see, e.g., Cunningham et al. 2019). The rates for the H white dwarfs, however, appear to be some of the highest among the other DAs at their temperature. This is especially the case with WD J1039 (Vanderbosch et al. 2020, estimated using Ca) and WD J1650+1443 (this work, using both Mg and Ca), for which the accretion rates are $\gtrsim 10^{10}\,\mathrm{g\,s^{-1}}$, making them some of the highest accretion rate DAs. The Mg-estimates accretion rate for WD J1237+5937 is

also quite high. Dusty white dwarfs usually have higher accretion rates, but none of the H transiting debris have detected dust disks. This motivates future searches for dust disks around these systems. With WD J1237+5937, however, it possible that we are measuring an historical average (thus higher) accretion rate, owing to its very low temperature and, thus, long diffusion timescales. For the other DAs, the diffusion timescales are very short and, therefore, we are likely measuring the instantaneous accretion rates.

The above indicates that the transiting debris systems tend to have higher accretion rates. The reason for this is not immediately clear. It is possible that these systems are in a more active state (which leads to active production of dust and debris, and thus we are more likely to observe transits), which leads to higher accretion rates. These high accretion rate DA white dwarfs may be the missing links between low rates in DA and high historical average rates in DBs: it is only at these most active stages that very high accretion rates are seen in DAs, which die off quickly owing to their small diffusion timescales. This argument may also indicate that the objects with high accretion rates are more likely to display transits from dust and debris, as the disk might get thickened due to the elevated activity (collisions, for example). This can then be used as a selection criterion for easier identification of transiting debris systems among large spectroscopic data sets. We also note here that assuming an accretion-diffusion equilibrium gives a lower limit of the accretion rates. If the objects are accreting vigorously and the metal abundances are on the rise, the true accretion rates are even higher than estimated in this way.

Another possibility is that the accretion rates in these systems are somehow being overestimated. This mainly translates to an overestimation in the metal abundances. This is possible if a significant portion of the metal absorption lines are of circumstellar origin and are being misidentified as photospheric. Such a possibility is already hinted at with the case of WD J1944+4557, where the totality of the Ca absorption line appears to be circumstellar. A detailed discussion of circumstellar absorption contribution in the context of WD 1145+017 already appears in Le Bourdais et al. (2024).

The current data, however, are not sufficient to test any of the above possibilities. This poses the need for the detection of more transiting debris systems and their in-depth analysis. We expect to detect several more such systems in both currently available data sets like Gaia (Z. P. Vanderbosch et al. 2025, in preparation), and also the more recent data releases in ZTF (J. van Roestel et al. 2025, in preparation), and upcoming surveys like the Large Synoptic Survey Telescope (LSST Rubin Observatory, Ivezić et al. 2019).

We acknowledge here some caveats associated with this preliminary comparison. This includes possible inconsistencies with abundance measurements from different works, or underestimation of accretion rates (Cunningham et al. 2019). A proper comparison would require re-analysis of all the available spectra with consistent atmosphere models, which is beyond the scope of this work. However, we do not expect these factors to change Figure 16 or the conclusions qualitatively. This is because (1) changes in accretion rate calculation will affect all the stars in a temperature bin equally, and (2) the variation in abundance measurements with different atmosphere models are likely to be much smaller ($\lesssim 0.3$ dex in most cases) than the span of the vertical axis in these figures.

7. Conclusions

We have performed a systematic search for white dwarfs with transiting planetary debris using the epochal photometric data from the ZTF DR10. Starting with the Gaia eDR3-based white dwarf catalog (Gentile Fusillo et al. 2021b), we applied variability metrics to the corresponding ZTF light curves to curate a list of highly variable white dwarfs. We then performed a visual inspection of the light curves of these objects to look for features characteristic of transiting debris (e.g., aperiodic variability and transit-like dips), and obtained optical spectroscopy of the most promising candidates. This led to the discovery of six strong candidates for white dwarfs with transiting planetary debris. We also performed follow-up high-speed time-series photometry to investigate the behavior of these candidates on short timescales (a few hours), revealing rapid variability in three out of six. Our methodology recovered all previously known transiting white dwarf systems, demonstrating the strong promise of our technique.

Most of the eight previously known transiting debris systems show sustained variability on short timescales (hours to days). Follow-up high-speed photometry confirmed this behavior for three of our six new candidates: WD J0923 +7326, WD J1302+1650, and WD J1944+4557. Four objects (including WD J1302+1650), however, display photometric variability over much longer timescales (spanning months to years). These objects, thus, potentially form their own subclass of variables. The erratic and large amplitude variability in WD J0923+7326 is intriguing, especially because it shows a long-duration brightening event which is not expected in such systems. For WD J1302+1650, owing to its short-timescale variability, the long-timescale features can be interpreted as overall changes in debris activity, with higher debris activity skewing the flux to lower values. The other two objects of this type, WD J1237+5937 and WD J1013−0427, do not display variability on short timescales (at least with the current data) but show prominent "transit"-like events lasting for $\simeq 4$ months and $\simeq 2$ yr, respectively. The reason behind their long-timescale activities is not clear, but can potentially arise from collision among large debris objects at wider orbits.

WD J1013−0427 is especially unique as it changes color during transit: the transit depth in the ZTF-r band is significantly shallower than in the g band. This is the first

report of reddening during transit in this class of objects. We conjecture that this results from the preferential scattering of blue light by small-sized dust grains. A simple radiative transfer model in the optically thin regime indicates the abundance of small dust grains of size $\simeq 0.2$–$0.3\,\mu$m in the obscuring material. Additionally, this system also shows metal emission lines in its optical spectrum (making this an even rarer object), indicative of a gas disk. The emission profile suggests that the disk is both eccentric and optically thick. We formulated a generalized disk model which incorporates both effects and fits the data well. We constrained several essential properties of the gas disk, namely the radial extent ($\approx 0.2 R_\odot$ to $\approx 0.5 R_\odot$) and eccentricity (≈ 0.25).

Owing to the limited number of systems found, we do not have sufficient information about the population-wide properties of white dwarfs showing transiting debris. We attempt to initiate such an analysis by comparing the inferred accretion rates of these systems to the broader pool of metal-polluted white dwarfs (Section 6). We show that transiting debris objects tend to exhibit relatively higher accretion rates, which is intriguing and demands future investigation. Another important parameter is the orbital radius of the debris, which can be inferred if the orbital period is known. The wild variations in the activity and morphology of the debris, even over timescales of a few days, makes inference of a recurrence period challenging. Only four objects have known orbital periods, but attempts are ongoing to search for periods in more of these systems. Another open question is about the presence of dust disks in these systems. Dust disks are expected, but their detection in these systems may be disfavored owing to the high viewing angle inclination. This is required to observe debris transits, but reduces the effective infrared emission area (see for example Equation (3) in Farihi 2016). With most of the known objects not having a reliable mid-infrared measurement (see Figure 17), the currently available data sets are far from sufficient to make any claims. But confirming the presence of dust disks in these systems would be essential, and require deeper infrared observations.

Going back to techniques to identify variable objects, we presented a novel method for shortlisting variables of interest from a pool of light curves. This is done by examining the object's position in a metric space defined by two variability metrics: von Neumann statistics (η, Equation (6)) and Pearson-Skew (S_P, Equation (7)). The former quantifies the randomness in the time-series data and the latter distinguishes between brightening and dimming events. In this work, we use this in our search for transiting planetary debris and show that the third quadrant defined by $\eta \lesssim 1.8$ and $S_P < 0$ is very promising in identifying such systems. We also discuss how variables of other types (like CVs showing outbursts) occupy different regions in this metric space. Thus, this space enables a "first guess" about the nature and timescale of the variability of the object. This guess applies not only to white dwarfs or transiting

debris systems, but the utility of this metric space can be easily extended to other systems showing photometric variability (see Bhattacharjee et al. 2025a for its application to the central stars of planetary nebulae). In the coming era of large photometric sky surveys (like the Rubin Observatory LSST), such simple metric spaces with easy interpretability will be especially effective at identifying astrophysically interesting sources.

We conclude by briefly discussing the scope for future discovery of more transiting debris candidates. In our work, we have a total of 14 transiting debris objects/candidates (with eight already known and the six new candidates from this work). Our starting sample of white dwarfs, which pass all the photometric quality cuts, consists of 56,065 objects. This leads to a very naive occurrence rate of at least $\simeq 0.03\%$. This is more than an order of magnitude lower than that predicted in Robert et al. (2024, even if we assume a conservative metal-pollution fraction). This gives a loose lower bound on the occurrence rate of transiting debris systems, but strongly indicates that many more such objects are yet to be found even in the data set used in this work. It also ignores the observed long-term variability (especially periods of dormancy) that complicate accurate calculations of occurrence rates (van Sluijs & Van Eylen 2018; Rowan et al. 2019; Robert et al. 2024; Hermes et al. 2025). We are in the process of obtaining follow-up observations of several other objects in our top 1% variables and in the third quadrant of η–S_P with the aim of finding more debris systems. We note here that the infrequent nature of the long-timescale dips in systems similar to those discovered in this work poses a difficulty to identifying them in data sets of short temporal baselines. Thus long baseline surveys like ZTF, and soon the Rubin Observatory's Legacy Survey of Space and Time, are instrumental to the detection and characterization of transiting debris at white dwarfs.

Appendix A
Gaia Quality Cuts

The astrometric cuts include a distance cut of 500 pc (using the inverse of the Gaia DR3 parallax) along with a minimum PARALLAX_OVER_ERROR> 10. We also use the cut of ASTROMETRIC_EXCESS_NOISE_SIG<2, which is recommended in Gentile Fusillo et al. (2021b) to generate a cleaner sample in terms of noise. We acknowledge an incompleteness in the selection procedure, which we recognized after the compilation of the results. In the above selection cuts, however, we have rejected objects with ASTROMETRIC_EXCESS_NOISE< 1 and ASTROMETRIC_EXCESS_NOISE_SIG> 2, which is undesirable. We checked that our Gaia sample increases to 121,967 (an increase of 5171 sources, i.e., by $\approx 4\%$) if the correct constraint is applied. However, even with the present cuts, we recovered all previously known transiting debris systems, along with the new candidates presented in this paper. Thus, we proceeded without re-doing the work to include the missing objects. Still, we acknowledge this limitation and that there can be additional debris candidates among wrongly rejected systems.

We apply the following photometric cuts: PHOT_BP_MEAN_MAG< 20.9, PHOT_BP_MEAN_FLUX_OVER_ERROR > 10, PHOT_RP_MEAN_FLUX_OVER_ERROR > 10, PHOT_G_MEAN_FLUX_OVER_ERROR > 50 and also the condition PHOT_PROC_MODE = 0 which marks the source which have complete color information. We also use the polynomial correction of the *BP/RP Excess Factor* with BP and RP magnitude as suggested in Riello et al. (2021) and use the conditions |BPRP_EXCESS_CORRECTED| < 2.0×SIGMA_BPRP_EXCESS and for the astrometric goodness of fit, we use the cut of ASTROMETRIC_CHI2_AL/ASTROMETRIC_N_GOOD_OBS_AL−5 < 1.44×max(1.0, exp(−0.4(PHOT_G_MEAN_MAG−19.5))).

Appendix B
Spectral Energy Distributions

Here we provide the spectral energy distributions (SEDs) of the six new candidate transiting debris systems. The SEDs were queried using the VizieR online photometry viewer tool[32] within a radius of $2''$ around the Gaia DR3 target coordinates. For consistency, we only show the photometry from the following catalogs: Lasker et al. (2008), Chambers et al. (2016), Schlafly et al. (2019), Paegert et al. (2021), which proved to be sufficient for our purpose. Furthermore, we discarded all data points without any quoted errors (which include WISE upper limits). The results are shown in Figure 17. We also over plot the best fit spectroscopic models. None of the objects have reliable mid-infrared photometry available, preventing any inference of possible infrared excess. WD J0923+7326 appears to have infrared excess in WISE W1 and W2 but close inspection shows significant blending with two nearby sources resolved in Pan-STARRS and Gaia. A $10''$ WISE catalog query around the target coordinate yields two objects with almost identical W1 and W2 fluxes (≈ 16 mag in W1 and ≈ 15.5 mag in W2). This substantiates the blended nature of the sources, rendering the measurements unreliable.

---

[32] http://vizier.cds.unistra.fr/vizier/sed/
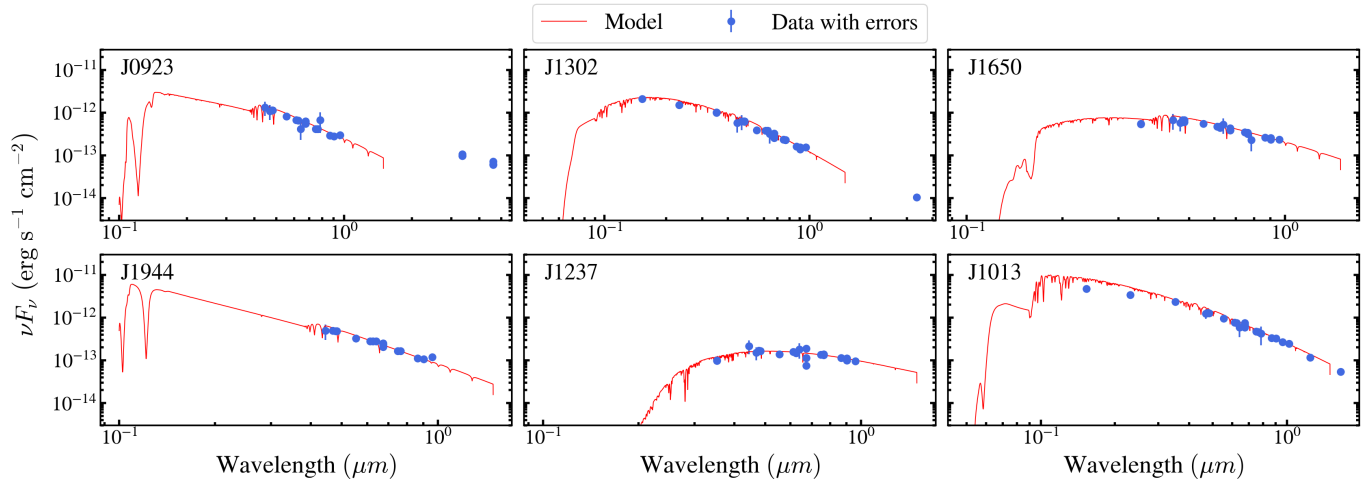
Figure 17. Spectral energy distributions of the six new transiting debris candidates. WD J0923+7326 appears to have infrared excess but close inspection shows the possibility of significant blending with two nearby sources. The others either do not have available infrared photometry or show any excess. Future deeper multiwavelength observations is required to study the presence of dust disks in these systems.

ORCID iDs

Soumyadeep Bhattacharjee ⓘ https://orcid.org/0000-0003-2071-2956

Zachary P. Vanderbosch ⓘ https://orcid.org/0000-0002-0853-3464

Mark A. Hollands ⓘ https://orcid.org/0000-0003-0089-2080

Pier-Emmanuel Tremblay ⓘ https://orcid.org/0000-0001-9873-0121

Siyi Xu (许偲艺) ⓘ https://orcid.org/0000-0002-8808-4282

Joseph A. Guidry ⓘ https://orcid.org/0000-0001-9632-7347

J. J. Hermes ⓘ https://orcid.org/0000-0001-5941-2286

Ilaria Caiazzo ⓘ https://orcid.org/0000-0002-4770-5388

Antonio C. Rodriguez ⓘ https://orcid.org/0000-0003-4189-9668

Jan van Roestel ⓘ https://orcid.org/0000-0002-2626-2872

Kareem El-Badry ⓘ https://orcid.org/0000-0002-6871-1752

Benjamin R. Roulston ⓘ https://orcid.org/0000-0002-9453-7735

Reed Riddle ⓘ https://orcid.org/0000-0002-0387-370X

Ben Rusholme ⓘ https://orcid.org/0000-0001-7648-4142

Steven L. Groom ⓘ https://orcid.org/0000-0001-5668-3507

Roger Smith ⓘ https://orcid.org/0000-0001-7062-9726

Odette Toloza ⓘ https://orcid.org/0000-0002-2398-719X

References

Allègre, C., Manhès, G., & Lewin, É. 2001, E&PSL, 185, 49
Astropy Collaboration, Price-Whelan, A. M., Sipőcz, B. M., et al. 2018, AJ, 156, 123
Astropy Collaboration, Robitaille, T. P., Tollerud, E. J., et al. 2013, A&A, 558, A33
Aungwerojwit, A., Gänsicke, B. T., Dhillon, V. S., et al. 2024, MNRAS, 530, 117
Bauer, E. B., & Bildsten, L. 2019, ApJ, 872, 96
Bédard, A., Bergeron, P., Brassard, P., & Fontaine, G. 2020, ApJ, 901, 93

Bellm, E. C., Kulkarni, S. R., Graham, M. J., et al. 2019, PASP, 131, 018002
Bhattacharjee, S., Kulkarni, S. R., Kong, A. K. H., et al. 2025a, PASP, 137, 024201
Bhattacharjee, S., Reindl, N., Bond, H. E., et al. 2025b, arXiv:2502.18651
Brouwers, M. G., Bonsor, A., & Malamud, U. 2022, MNRAS, 509, 2404
Budaj, J., Bernhard, K., Jones, D., & Munday, J. 2025, NatAs, 9, 380
Chambers, K. C., Magnier, E. A., Metcalfe, N., et al. 2016, arXiv:1612.05560
Cody, A. M., Stauffer, J., Baglin, A., et al. 2014, AJ, 147, 82
Córsico, A. H., Althaus, L. G., Miller Bertolami, M. M., & Kepler, S. O. 2019, A&ARv, 27, 7
Cunningham, T., Tremblay, P.-E., Freytag, B., Ludwig, H.-G., & Koester, D. 2019, MNRAS, 488, 2503
Debes, J. H., Kilic, M., Faedi, F., et al. 2012, ApJ, 754, 59
Debes, J. H., & Sigurdsson, S. 2002, ApJ, 572, 556
Dennihy, E., Farihi, J., Fusillo, N. P. G., & Debes, J. H. 2020a, ApJ, 891, 97
Dennihy, E., Xu, S., Lai, S., et al. 2020b, ApJ, 905, 5
Dhillon, V. S., Marsh, T. R., Stevenson, M. J., et al. 2007, MNRAS, 378, 825
Drake, A. J., Djorgovski, S. G., Mahabal, A., et al. 2009, ApJ, 696, 870
Dufour, P., Blouin, S., Coutu, S., et al. 2017, in ASP Conf. Ser. 509, 20th European White Dwarf Workshop, ed. P. E. Tremblay, B. Gaensicke, & T. Marsh (San Francisco, CA: ASP), 3
Dufour, P., Kilic, M., Fontaine, G., et al. 2010, ApJ, 719, 803
Farihi, J. 2016, NewAR, 71, 9
Farihi, J., Gänsicke, B. T., & Koester, D. 2013, Sci, 342, 218
Farihi, J., Gänsicke, B. T., Wyatt, M. C., et al. 2012, MNRAS, 424, 464
Farihi, J., Zuckerman, B., & Becklin, E. E. 2008, ApJ, 674, 431
Farihi, J., Hermes, J. J., Marsh, T. R., et al. 2022, MNRAS, 511, 1647
Flewelling, H. A., Magnier, E. A., Chambers, K. C., et al. 2020, ApJS, 251, 7
Foreman-Mackey, D., Conley, A., Meierjurgen Farr, W., et al. 2013, emcee: The MCMC Hammer, Astrophysics Source Code Library, ascl:1303.002
Gänsicke, B. T., Marsh, T. R., Southworth, J., & Rebassa-Mansergas, A. 2006, Sci, 314, 1908
Genest-Beaulieu, C., & Bergeron, P. 2019, ApJ, 882, 106
Gentile Fusillo, N. P., Manser, C. J., Gänsicke, B. T., et al. 2021a, MNRAS, 504, 2707
Gentile Fusillo, N. P., Tremblay, P.-E., Gänsicke, B. T., et al. 2019, MNRAS, 482, 4570
Gentile Fusillo, N. P., Tremblay, P. E., Cukanovaite, E., et al. 2021b, MNRAS, 508, 3877
Ginsburg, A., Sipőcz, B. M., Brasseur, C. E., et al. 2019, AJ, 157, 98
Goksu, O. A., Kutra, T., & Wu, Y. 2024, AJ, 167, 236
Gordon, K. D., Clayton, G. C., Decleir, M., et al. 2023, ApJ, 950, 86

Guidry, J., Hermes, J., & Vanderbosch, Z. 2024, AAS/Division for Extreme Solar Systems Abstracts, 56, 612.01
Guidry, J. A., Hermes, J. J., De, K., et al. 2024, ApJ, 972, 126
Guidry, J. A., Vanderbosch, Z. P., Hermes, J. J., et al. 2021, ApJ, 912, 125
Hallakoun, N., Xu, S., Maoz, D., et al. 2017, MNRAS, 469, 3213
Hansen, J. E. 1971, JAtS, 28, 1400
Harding, L. K., Hallinan, G., Milburn, J., et al. 2016, MNRAS, 457, 3036
Harris, C. R., Millman, K. J., van der Walt, S. J., et al. 2020, Natur, 585, 357
Hermes, J. J., Guidry, J. A., Vanderbosch, Z. P., et al. 2025, ApJ, 980, 56
Hillenbrand, L. A., Kiker, T. J., Gee, M., et al. 2022, AJ, 163, 263
Hodgkin, S. T., Harrison, D. L., Breedt, E., et al. 2021, A&A, 652, A76
Horne, K., & Marsh, T. R. 1986, MNRAS, 218, 761
Hunter, J. D. 2007, CSE, 9, 90
Inight, K., Gänsicke, B. T., Breedt, E., et al. 2023, MNRAS, 524, 4867
Ivezić, Ž., Kahn, S. M., Tyson, J. A., et al. 2019, ApJ, 873, 111
Izquierdo, P., Rodríguez-Gil, P., Gänsicke, B. T., et al. 2018, MNRAS, 481, 703
Janes, K. A., Clemens, D. P., Hayes-Gehrke, M. N., et al. 2004, AAS Meeting, 204, 10.1
Jiménez-Esteban, F. M., Torres, S., Rebassa-Mansergas, A., et al. 2018, MNRAS, 480, 4505
Jura, M. 2003, ApJL, 584, L91
Jura, M., Farihi, J., & Zuckerman, B. 2007, ApJ, 663, 1285
Kanaan, A., Kepler, S. O., & Winget, D. E. 2002, A&A, 389, 896
Kenworthy, M., Lock, S., Kennedy, G., et al. 2023, Natur, 622, 251
Kilic, M., Kosakowski, A., Moss, A. G., Bergeron, P., & Conly, A. A. 2021, ApJL, 923, L6
Kleinman, S. J., Kepler, S. O., Koester, D., et al. 2013, ApJS, 204, 5
Koester, D. 2010, MmSAI, 81, 921
Koester, D., Gänsicke, B. T., & Farihi, J. 2014, A&A, 566, A34
Koester, D., Kepler, S. O., & Irwin, A. W. 2020, A&A, 635, A103
Lai, S., Dennihy, E., Xu, S., et al. 2021, ApJ, 920, 156
Lasker, B. M., Lattanzi, M. G., McLean, B. J., et al. 2008, AJ, 136, 735
Le Bourdais, É., Dufour, P., & Xu, S. 2024, ApJ, 977, 93
Magnier, E. A., Chambers, K. C., Flewelling, H. A., et al. 2020, ApJS, 251, 3
Malamud, U., Grishin, E., & Brouwers, M. 2021, MNRAS, 501, 3806
Mandigo-Stoba, M. S., Fremling, C., & Kasliwal, M. 2022a, JOSS, 7, 3612
Mandigo-Stoba, M. S., Fremling, C., & Kasliwal, M. 2022b, DBSP_DRP: A Python Package for Automated Spectroscopic Data Reduction of DBSP Data, v1.0.0, Zenodo, doi:10.5281/zenodo.6241526
Manser, C. J., Gänsicke, B. T., Gentile Fusillo, N. P., et al. 2020, MNRAS, 493, 2127
Manser, C. J., Gänsicke, B. T., Marsh, T. R., et al. 2016, MNRAS, 455, 4467
Masci, F. J., Laher, R. R., Rusholme, B., et al. 2019, PASP, 131, 018003
Mathis, J. S., Rumpl, W., & Nordsieck, K. H. 1977, ApJ, 217, 425
Meisner, A. M., Lang, D., & Schlegel, D. J. 2018, AJ, 156, 69
Melis, C., Farihi, J., Dufour, P., et al. 2011, ApJ, 732, 90
Melis, C., Jura, M., Albert, L., Klein, B., & Zuckerman, B. 2010, ApJ, 722, 1078
Mullally, F., Kilic, M., Reach, W. T., et al. 2007, ApJS, 171, 206
Naylor, T. 1998, MNRAS, 296, 339
Ochsenbein, F., Bauer, P., & Marcout, J. 2000, A&AS, 143, 23
Oke, J. B., Cohen, J. G., Carr, M., et al. 1995, PASP, 107, 375
Oke, J. B., & Gunn, J. E. 1982, PASP, 94, 586
Ould Rouis, L. B., Hermes, J. J., Gänsicke, B. T., et al. 2024, ApJ, 976, 156
Owens, D., Xu, S., Manjavacas, E., et al. 2023, AJ, 166, 5
Paegert, M., Stassun, K. G., Collins, K. A., et al. 2021, arXiv:2108.04778
Perley, D. A. 2019, PASP, 131, 084503
Prochaska, J., Hennawi, J., Cooke, R., et al. 2020a, pypeit/PypeIt: Release v1.0.0, Zenodo, doi:10.5281/zenodo.3743493

Prochaska, J., Hennawi, J., Westfall, K., et al. 2020b, JOSS, 5, 2308
Putirka, K. D., & Xu, S. 2021, NatCo, 12, 6168
Rappaport, S., Gary, B. L., Kaye, T., et al. 2016, MNRAS, 458, 3904
Redfield, S., Farihi, J., Cauley, P. W., et al. 2017, ApJ, 839, 42
Reindl, N., Islami, R., Werner, K., et al. 2023, A&A, 677, A29
Reindl, N., Schaffenroth, V., Filiz, S., et al. 2021, A&A, 647, A184
Riello, M., De Angeli, F., Evans, D. W., et al. 2021, A&A, 649, A3
Rigault, M. 2018, ztfquery, a Python Tool to Access ZTF Data, Zenodo, doi:10.5281/zenodo.1345222
Ritter, H., & Kolb, U. 2003, A&A, 404, 301
Rivera Sandoval, L. E., & Maccarone, T. J. 2019, MNRAS, 483, L6
Rivera Sandoval, L. E., Maccarone, T. J., Cavecchi, Y., Britt, C., & Zurek, D. 2021, MNRAS, 505, 215
Rivera Sandoval, L. E., Maccarone, T. J., & Pichardo Marcano, M. 2020, ApJL, 900, L37
Roberson, M. S., Fremling, C., & Kasliwal, M. M. 2021, DBSP_DRP: DBSP Data Reduction Pipeline, Astrophysics Source Code Library, ascl:2108.020
Robert, A., Farihi, J., Van Eylen, V., et al. 2024, MNRAS, 533, 1756
Rockosi, C., Stover, R., Kibrick, R., et al. 2010, Proc. SPIE, 7735, 77350R
Rodriguez, A. C., Mróz, P., Kulkarni, S. R., et al. 2022, ApJ, 927, 150
Rogers, L. K., Bonsor, A., Xu, S., et al. 2024, MNRAS, 527, 6038
Romero, A. D., Kepler, S. O., Hermes, J. J., et al. 2022, MNRAS, 511, 1574
Rowan, D. M., Tucker, M. A., Shappee, B. J., & Hermes, J. J. 2019, MNRAS, 486, 4574
Schlafly, E. F., Meisner, A. M., & Green, G. M. 2019, ApJS, 240, 30
Sheinis, A. I., Bolte, M., Epps, H. W., et al. 2002, PASP, 114, 851
Shingles, L., Smith, K. W., Young, D. R., et al. 2021, TNSAN, 7, 1
Steele, A., Debes, J., Xu, S., Yeh, S., & Dufour, P. 2021, ApJ, 911, 25
Swan, A., Farihi, J., Melis, C., et al. 2023, MNRAS, 526, 3815
The pandas development team 2020, pandas-dev/pandas: Pandas, latest v1.5.3, Zenodo, doi:10.5281/zenodo.3509134
Tran, V., De, K., & Hillenbrand, L. 2024, MNRAS, 530, 2076
Tremblay, P. E., Ludwig, H. G., Steffen, M., & Freytag, B. 2013, A&A, 559, A104
van Sluijs, L., & Van Eylen, V. 2018, MNRAS, 474, 4603
Vanderbosch, Z. 2022, zvanderbosch/phot2lc: phot2lc v1.7.0 release, Zenodo, doi:10.5281/zenodo.6459216
Vanderbosch, Z., Hermes, J. J., Dennihy, E., et al. 2020, ApJ, 897, 171
Vanderbosch, Z. P., Hermes, J. J., Winget, D. E., et al. 2022, ApJ, 927, 158
Vanderbosch, Z. P., Rappaport, S., Guidry, J. A., et al. 2021, ApJ, 917, 41
Vanderburg, A., Johnson, J. A., Rappaport, S., et al. 2015, Natur, 526, 546
Vincent, O., Bergeron, P., & Lafrenière, D. 2020, AJ, 160, 252
Virtanen, P., Gommers, R., Oliphant, T. E., et al. 2020, NatMe, 17, 261
Wang, L., Zhang, X., Wang, J., et al. 2023, ApJ, 944, 23
Wilson, T. G., Farihi, J., Gänsicke, B. T., & Swan, A. 2019, MNRAS, 487, 133
Xu, S., Dufour, P., Klein, B., et al. 2019a, AJ, 158, 242
Xu, S., Hallakoun, N., Gary, B., et al. 2019b, AJ, 157, 255
Xu, S., Jura, M., Dufour, P., & Zuckerman, B. 2016, ApJL, 816, L22
Xu, S., Lai, S., & Dennihy, E. 2020, ApJ, 902, 127
Xu, S., Rappaport, S., van Lieshout, R., et al. 2018, MNRAS, 474, 4795
Xu, S., Yeh, S., Rogers, L. K., et al. 2024, AJ, 167, 248
Zuckerman, B., & Becklin, E. E. 1987, Natur, 330, 138
Zuckerman, B., Koester, D., Melis, C., Hansen, B. M., & Jura, M. 2007, ApJ, 671, 872
Zuckerman, B., Koester, D., Reid, I. N., & Hünsch, M. 2003, ApJ, 596, 477
Zuckerman, B., Melis, C., Klein, B., Koester, D., & Jura, M. 2010, ApJ, 722, 725